Computer Methods in Applied Mechanics and Engineering 432 (2024) 117414

Contents lists available at ScienceDirect

Comput. Methods Appl. Mech. Engrg.

journal homepage: www.elsevier.com/locate/cma

A symmetric interior-penalty discontinuous Galerkin isogeometric analysis spatial discretization of the self-adjoint angular flux form of the neutron transport equation

S.G. Wilson [a,b,*], M.D. Eaton [a], J. Kópházi [c,a]

[a] Nuclear Engineering Group, Department of Mechanical Engineering, City and Guilds Building, Imperial College London, Exhibition Road, South Kensington, London, SW7 2BX, United Kingdom
[b] Rolls-Royce plc, PO BOX 2000, Derby, DE21 7XX, UK
[c] Institute of Nuclear Techniques, Budapest University of Technology and Economics, Mű,egyetem rkp. 3, Budapest, 1111, Hungary

ARTICLE INFO

Dataset link: https://doi.org/10.5281/zenodo.11863256

Keywords:
Self-Adjoint Angular Flux (SAAF)
Multi-group neutron transport equation
Discrete ordinates (S_N)
Interior-penalty scheme
Discontinuous galerkin
Isogeometric analysis

ABSTRACT

This paper presents the first application of a symmetric interior-penalty discontinuous Galerkin isogeometric analysis (SIP-DG-IGA) spatial discretization to the self-adjoint angular flux (SAAF) form of the multi-group neutron transport equation. The penalty parameters are determined, for general element types, from a mathematically rigorous coercivity analysis of the bilinear form. The proposed scheme produces a compact spatial discretization stencil. It also yields symmetric positive-definite (SPD) matrices, which can be efficiently solved using pre-conditioned conjugate gradient (PCG) solution algorithms. The proposed discretization scheme is verified using the method of manufactured solutions (MMS) and several nuclear reactor physics benchmark verification test cases. For sufficiently smooth elliptic problems, the proposed spatial discretization can exploit higher-order continuity, or k-refinement, of the NURBS basis to consistently yield greater numerical accuracy per degree of freedom (DoF) than standard h-refinement. Since this is a discontinuous scheme, it can also accurately model significant changes in the neutron scalar flux that may occur near the material interfaces of heterogeneous problems.

1. Introduction

The neutron transport equation (NTE) is a linearized form of the full non-linear Boltzmann transport equation from the kinetic theory of gases [1]. The NTE determines the mean, or expected, value of the neutron distribution within a seven-dimensional phase space of position (x, y, z), energy (E); angle (θ, φ) and time (t). It models the migration and interaction of neutrons through nuclear reactor cores and radiation shields. The NTE assumes that neutrons are point particles; that they travel in straight lines between collisions; that collisions are instantaneous; that neutron–neutron interactions are negligible; and that material properties are isotropic [2]. It was first derived by Ornstein and Uhlenbeck [3]; and its modern form was conceived by Halpern, Lueneburg and Clark [4]. It can be rigorously derived from quantum mechanical considerations using the quantum Liouville equation [5]; or from statistical approaches using master equations [6]. The first-order form of the neutron transport (FONT) equation is a linear hyperbolic partial integro-differential equation (PIDE). It may be re-formulated into alternative, yet equivalent, forms such as the second-order even-parity (EP) and odd-parity (OP) equations [7]; the weighted-least squares (WLS) equation [8]; and the self-adjoint angular flux (SAAF) formulation [9].

* Corresponding author at: Nuclear Engineering Group, Department of Mechanical Engineering, City and Guilds Building, Imperial College London, Exhibition Road, South Kensington, London, SW7 2BX, United Kingdom.
E-mail address: seth.wilson16@imperial.ac.uk (S.G. Wilson).

https://doi.org/10.1016/j.cma.2024.117414
Received 5 July 2024; Received in revised form 15 September 2024; Accepted 19 September 2024
Available online 26 September 2024

Second-order forms of the NTE are linear elliptic PIDEs [10,11]. When spatially discretized using continuous Bubnov–Galerkin methods, the EP and the SAAF equations yield matrices that are symmetric positive-definite (SPD). These SPD matrices enable the use of computationally efficient matrix-solution methods; e.g. the pre-conditioned conjugate gradient (PCG) iteration and multi-level, or multi-grid, solution algorithms. The focus of this paper is the SAAF form of the NTE, which is spatially discretized using a higher-order accurate symmetric interior-penalty isogeometric analysis (SIP-DG-IGA) scheme, which yields a compact spatial discretization stencil and SPD matrices. Such spatial discretization methods have advantageous numerical properties when solved on the latest high-performance computing (HPC) hardware architectures. The Center for Efficient Exa-scale Discretizations (CEED) program of research has demonstrated that higher-order spatial discretizations are more-computationally efficient than lower-order methods on the latest HPC hybrid multi-core CPU and many-core GPU hardware architectures [12]. For these HPC hardware architectures, memory bandwidth is one of the most important aspects in determining optimal computational performance [13]. Moreover, as the number of cores in the CPUs, or GPUs, increase, and as the memory hierarchy becomes more complex, the data has to be managed more efficiently by optimizing the cache usage [14]. Therefore, it is important to develop methods that minimize indirection and cache misses, which can improve computational efficiency [15]. Higher-order spatial discretizations, such as the scheme presented in this paper, can utilize dense matrix operations that have more-compact memory footprints than sparse matrix operations [16].

Along with the advances in HPC hardware architectures, the need to simplify the computer-aided geometric design (CAGD) boundary representation (B-rep) in the computer-aided engineering (CAE) pipeline is leading to the development of higher-order finite element methods (FEM) [17,18]; spectral element methods (SEM) [19]; isogeometric analysis (IGA) [20–23]; and virtual element methods (VEM) [24,25]. Such higher-order methods are capable of representing geometrically complex curvilinear geometries and computational domains. In addition, such approaches are able to produce curvilinear geometric multi-level and multi-grid matrix-solution algorithms using geometrically hierarchical curvilinear computational meshes [26]. More recently, such methods have been implemented in energy-dependent, curvilinear self-adaptive algorithms for nuclear reactor physics problems using dual-weighted residual error measures [21,27,28].

In this paper, the energy variable of the SAAF form of the NTE is dicretized using the standard multi-group approximation; its modern form was conceived by Hurwitz and Ehrlich [29]. This reduces the PIDE into a discrete set of weakly-coupled PDEs, which may be spatially discretized. The angular variable is discretized using the discrete-ordinates (S_N) method [30]; its modern form was conceived by Carlson and Lee [31,32].

Elliptic PDEs govern equilibrium problems and the discretized system is best solved using relaxation methods. However, elliptic PDEs, when used to model transport-dominated phenomena, may violate causality [33]. The EP and OP equations allow for a reduction in the number of angular unknowns to solve for, which can improve computational efficiency [7]. However, the even and odd parity contributions to the angular flux are coupled at vacuum boundaries [11]. The SAAF formulation solves for all contributions to the angular flux, which, although more computationally demanding, does allow for a more-accurate representation near vacuum boundaries [9]. Therefore, incoming boundary conditions can be treated in a manner similar to that of a standard S_N discretization of the FONT (FONT-S_N) equation. Moreover, for rectangular Cartesian coordinate systems, each discrete angular direction can be solved for *independently*; and therefore, the SAAF-S_N equation is compatible with the standard source iteration procedure [23].

An obvious shortcoming, however, shared by many second-order forms, is the singular behavior $1/\Sigma_t \to \infty$ as $\Sigma_t \to 0$ [34]; viz. the SAAF-S_N equation is not readily applicable to problems with vacuum regions without some form of void treatment [11]. However, this usually comes at the sacrifice of desirable properties. For example, Wang et al. and separately, Schunert et al. modified the bilinear form of their SAAF-S_N equation to ensure void-compatibility of the Rattlesnake code within the MOOSE framework [35,36]. Although the discretization tends towards that of the FONT-S_N equation and admits discrete adjoint-consistency in the fine-mesh limit, $h \to 0$, the modified bilinear form is asymmetric and the stabilization depends upon some free-floating parameter, which may require tuning. Morel and McGhee also derived a void-compatible SAAF formulation; however, their formulation did not constitute a statement of particle conservation [11].

1.1. Causality

Causality is a rigorous mathematical property of transport-dominated phenomena, which can be represented by systems of hyperbolic PDEs; e.g. neutron transport and Euler gas dynamics [2]. Causality, for such problems, means that information only travels downstream along characteristic directions, or along the paths in which discontinuities may propagate; e.g. shocks in gas dynamics [37]. However, there are circumstances where causality may be violated numerically. Whilst such non-physical behavior is generally considered to be a *coarse-mesh* problem, which may improve under refinement, it is one that affects many of the second-order forms of the NTE [33].

Each of the different forms of the steady-state NTE is a linear PIDE with respect to space. In a manner analogous to that of classifying conic sections, one may classify a PIDE by the discriminant of its characteristic equation. A first-order PDE is *hyperbolic* if real distinct characteristics exist; whereas a second-order PDE is *elliptic* if no real characteristics exist because they are imaginary. This serves to characterize *two* distinct types of problems: *propagation* and *equilibrium* problems. Physical systems governed by PDEs that have real characteristics are propagation problems; and thus, hyperbolic PDEs govern propagation problems. In contrast, physical problems governed by PDEs that have complex characteristics are equilibrium problems; and thus, elliptic PDEs govern equilibrium problems.

Should no real characteristics exist, then there exist no preferred, nor meaningful, paths along which physical information should propagate; this is characteristic of steady-state diffusion-like problems, where some perturbation is dissipated in all directions.

Consequently, the *domain of dependence* and the *range of influence* of every point coincide with the entire solution domain; wherein lies the violation of causality [38]. In other words, the solution at every point depends upon the solution at all other points and the solution at each point influences the solution at all other points. Therefore, an appropriate solution strategy should ensure that all internal requirements and auxiliary conditions are satisfied simultaneously.

This paper is based upon the author's PhD thesis [39]; and it extends the work of Wilson et al. [28,40]. They employed a symmetric interior penalty (SIP) scheme for a discontinuous Galerkin (DG) IGA spatial discretization of the multi-group neutron diffusion equation (NDE). Continuity in the numerical solution is weakly enforced between adjacent elements by penalization. This paper presents the first application of a SIP-DG spatial discretization to the multi-group SAAF-S_N equation. The penalty parameters are computed, for general element types, from a mathematically rigorous coercivity analysis of the bilinear form.

This paper is organized as follows: Section 2 introduces the mathematical description of a NURBS-based IGA spatial discretization; and the multi-group SAAF-S_N equation is presented in Section 3. The weak form of the SIP-DG-IGA SAAF-S_N equation is derived in Section 4; and in Section 4.1, penalty parameters are computed from trace inequality constants (TICs) for general element types from a coercivity analysis of the bi-linear form using the approach by Owens et al. [41]. Finally, numerical results are presented in Section 5. A series of nuclear reactor physics benchmark verification test cases are used to determine the computational accuracy of the proposed discretization; and the method of manufactured solutions (MMS) is used to compare the observed rates of convergence against optimal, theoretical ones.

2. A NURBS-based IGA spatial discretization

For many engineering problems, the complex surfaces bounding solid objects (boundary representation, or B-rep) can be described by bases of NURBS functions, or some other related spline-based description. The simplest description of the geometry is typically based upon a decomposition of the problem into its constituent material regions. Regardless, the physical domain can be exactly represented by a tessellation of NURBS patches, the union of which forms the physical mesh, $\mathcal{T}(V)$. The geometrical mapping is a parametrization of $\vec{r}:\hat{V}\rightarrow V$, which takes a point in the parametric domain, $\vec{r}^{-1}\in\hat{V}\subset\mathbb{R}^{\hat{d}}$, where the NURBS basis is defined, and maps it to a point in Euclidean space, $\vec{r}\in V\subset\mathbb{R}^{d}$, for $d,\hat{d}=1,2$ or 3.

A NURBS basis function defined over the real physical space, $R(\vec{r})$, is the composition of that function, $R(\vec{r}^{-1})$, with the inverse of the geometrical mapping; i.e. $R(\vec{r})=\{R(\vec{r}^{-1})\circ\vec{r}^{-1}:\forall\,\vec{r}^{-1}\in\hat{V}\}$. The parametric domain is local to a given patch. Consequently, a NURBS basis function has finite local support on a single given patch, in both $\hat{V}$ and V, as per the bijective mapping; i.e.:

$$\operatorname{supp}(R)=\left\{\vec{r}\in V_e:R(\vec{r})\neq 0,\forall\,\vec{r}^{-1}\in\hat{V}_e\right\},\quad\forall V_e\in\mathcal{T}(V). \tag{1}$$

Multi-dimensional, $d>1$, NURBS basis functions are constructed in a tensor-product fashion from univariate B-splines, which can be expressed via the Cox-de Boor recursion formula [42,43]. A description of the parametric domain, denoted by some parameter $0\leq\xi\leq 1$ in 1D, begins with an open knot-vector, Ξ_ξ, which is a set of non-decreasing coordinates: $\Xi_\xi=\{\xi_i\}_{i=1}^{n+p+1}$, where ξ_i are the knots; p is the polynomial degree of the basis; and n is the total number of basis functions that span ξ. Knots are points of reduced continuity that partition the parametric domain into knot-spans; the ith knot-span is defined by the half-closed interval $[\xi_i,\xi_{i+1})$. A knot-value is said to have a multiplicity of $\dot{m}$ knots if $\dot{m}$ number of knots take on the same value. The continuity of the basis over any given knot-value is $C^{p-\dot{m}}$. Within knot-spans of non-zero length, the basis is infinitely differentiable, C^∞-continuous; i.e. for $\xi_i\neq\xi_{i+1}$.

Increasing the multiplicity of a knot to $\dot{m}=p$ renders the NURBS basis interpolatory at that given knot-value. Effectively, a new patch boundary is formed and C^0-continuity is naturally enforced across the new boundary. For $\dot{m}=p+1$, again, a new patch boundary is formed. However, now, the basis is discontinuous, or C^{-1}-continuous.

The support of B-splines, $\{N_i^p\}_{i=1}^N$, is compact and extends over $p+1$ knot-spans; i.e. for $i=1,\ldots,N$:

$$\operatorname{supp}\left(N_i^p\right)=\left\{\xi\in\hat{V}\subset\mathbb{R}^1:N_i^p(\xi)\neq 0,\forall\,\xi_i\leq\xi<\xi_{i+p+1}\right\}; \tag{2}$$

and $p+1$ functions always have support within any given knot-span.

Eq. (3) expresses the tensor-product fashion in which bi-variate NURBS basis functions, $R_{i,j}^{p,q}(\xi,\eta)$, are formed from sets of univariate B-splines, $\{N_i^p(\xi)\}_{i=1}^N$ and $\{M_j^q(\eta)\}_{j=1}^M$. Respectively, the polynomial degrees of each set of univariate B-splines are denoted by p and q; and the knot-vectors are denoted by $\Xi_\xi=\{\xi_i\}_{i=1}^{N+p+1}$ and $\Xi_\eta=\{\eta_j\}_{j=1}^{M+q+1}$.

Each NURBS basis function corresponds to a *control-point*, a vector-valued coefficient. The set of control-points serves as the *scaffolding* for the problem geometry; that is the control-net, $\mathcal{B}=\{\vec{B}_{i,j}\}_{i,j=1}^{N,M}\subset\mathbb{R}^2$ in 2D. A NURBS object, $V\in\mathbb{R}^d$, is the piecewise projective transformation of a B-spline object in $\mathbb{R}^{d+1}$. The latter is defined as a set of projective control-points, to each of which is attributed a weight; i.e. $\mathcal{W}=\{W_{i,j}\}_{i,j=1}^{N,M}\subset\mathbb{R}$ in 2D. The control-points in the real physical space are obtained by dividing each of the projective control-points by its respective weight. These weights convey a sense of *affinity* for the control-points in the real physical space. This same transformation is applied to every point in the projective space. The NURBS basis functions are rendered rational by the division of the polynomial weighting function, the denominator of Eq. (3); i.e. for $i,j=1,\ldots,N,M$:

$$R_{i,j}^{p,q}(\xi,\eta)=\frac{N_i^p(\xi)M_j^q(\eta)W_{i,j}}{\sum_{i\prime=1}^{N}\sum_{j\prime=1}^{M}N_{i\prime}^p(\xi)M_{j\prime}^q(\eta)W_{i\prime,j\prime}}. \tag{3}$$

The NURBS basis functions are point-wise non-negative for non-negative weights.

The parametrization, $\vec{r}:\hat{V}\rightarrow V$, can now be defined as the linear combination of NURBS basis functions and control-points that define a surface, S:

$$S(\xi,\eta)=\sum_{i=1}^{N}\sum_{j=1}^{M}\vec{B}_{i,j}R_{i,j}^{p,q}(\xi,\eta),\quad \forall\,\xi,\eta\in\hat{V}. \tag{4}$$

The gradient over the domain with respect to the parametric space, $\hat{\nabla}$, can be expressed in terms of partial derivatives of the B-splines; but the gradient over the domain with respect to the real physical space, $\vec{\nabla}$, must be expressed as:

$$\underline{\mathbf{J}}_V\cdot\vec{\nabla}R_i^{p,q}(\xi,\eta)=\hat{\nabla}R_i^{p,q}(\xi,\eta),\quad \text{for } i=1,\ldots,N\times M. \tag{5}$$

The convention of the gradient operator is retained with the unit-vectors defined parallel to each of the axes in a rectangular Cartesian coordinate system; i.e. for $\vec{e}_\xi=\vec{e}_x=[1,0]^T$ and $\vec{e}_\eta=\vec{e}_y=[0,1]^T$:

$$\hat{\nabla}\equiv\vec{e}_\xi\frac{\partial}{\partial\xi}+\vec{e}_\eta\frac{\partial}{\partial\eta}. \tag{6}$$

The volumetric Jacobian (2×2)-matrix, is defined below:

$$\underline{\mathbf{J}}_V:=\begin{pmatrix}\partial x/\partial\xi & \partial y/\partial\xi\\ \partial x/\partial\eta & \partial y/\partial\eta\end{pmatrix}. \tag{7}$$

Stability of the discretization necessitates the mapping to be invertible and non-singular, $\det\underline{\mathbf{J}}_V>0$, almost everywhere, such that the NURBS basis functions are square-integrable.

One way in which to enrich the parametric domain is to form additional non-zero knot-spans. Knots can be inserted with a multiplicity of *one*, KI-1-refinement, up to p+1, KI-h-refinement. The latter is analogous to h-refinement in a standard FEM because the basis is reduced to C^0-continuity across the newly-formed element boundaries. Another way in which to enrich the basis is by degree-elevation (*DE*), which is analogous to p-refinement in a standard FEM. One notes that the refinement processes of *KI* and *DE* are not commutative [44].

3. The self-adjoint angular flux form of the multi-group neutron transport equation

This paper only considers the time-independent neutron transport, which is commonly used to analyze steady-state nuclear reactor physics, nuclear criticality and radiation shielding problems. More specifically, the self-adjoint angular flux (SAAF) form of the NTE is the focus of this paper. The energy domain is discretized using the multi-group approximation; the angular domain is discretized using the discrete ordinates (S_N) approximation; and the spatial domain is discretized using NURBS-based isogeometric analysis (IGA).

The continuous energy domain, $(E_{min},E_{max}]$, is partitioned into distinct values, $E_{max}=E_0>E_1>\ldots>E_G=E_{min}$, forming G number of energy groups; such that the gth-group spans the half-closed interval $(E_g,E_{g-1}]$. A *backward* indexing of the energy groups reflects the fact that most neutrons scatter progressively downwards in energy as they slow down [45].

Any integrals over the entire energy spectrum can now be expressed as a sum of individual integrals over each energy group; i.e.:

$$\int_0^\infty dE\approx\int_{E_G}^{E_0}dE\Rightarrow\sum_{g=1}^{G}\int_{E_g}^{E_{g-1}}dE. \tag{8}$$

The defining equation is integrated over each energy group and the result is solved for the multi-group components of the neutron angular flux, φ^{gk} for $k=1,\ldots,K$; where:

$$\varphi^{gk}(\vec{r})=\int_{E_g}^{E_{g-1}}\varphi^k(\vec{r},E)\,dE. \tag{9}$$

3.1. The multi-group SAAF-S_N equation

The multi-group SAAF-S_N equation is posed on a multi-dimensional closed, connected and bounded domain, $V\subset\mathbb{R}^d$, in the real physical space for $d=2,3$. The strong form of the problem is cast as solving $\varphi^{gk}:V\rightarrow\mathbb{R}$ for $g=1,\ldots,G$ and for $k=1,\ldots,K$:

$$\begin{cases}
-\vec{\Omega}^k\cdot\vec{\nabla}\dfrac{1}{\Sigma_t^g(\vec{r})}\vec{\Omega}^k\cdot\vec{\nabla}\varphi^{gk}(\vec{r})+\Sigma_t^g(\vec{r})\varphi^{gk}(\vec{r})=q^{gk}(\vec{r})-\vec{\Omega}^k\cdot\vec{\nabla}\dfrac{1}{\Sigma_t^g(\vec{r})}q^{gk}(\vec{r}), & \vec{r}\in V; \quad \text{(a)}\\
\varphi^{gk}(\vec{r})=0, & \vec{r}\in\partial V_V^-; \quad \text{(b)}\\
\varphi^{gk}(\vec{r})=\varphi^{gk\prime}(\vec{r}), & \vec{r}\in\partial V_R^-; \quad \text{(c)}\\
\varphi^{gk}(\vec{r})=\dfrac{1}{\Sigma_t^g(\vec{r})}\left[-\vec{\Omega}^k\cdot\vec{\nabla}\varphi^{gk}(\vec{r})+q^{gk}(\vec{r})\right], & \vec{r}\in\partial V_{ext}^+. \quad \text{(d)}
\end{cases} \tag{10}$$

The normal vector, $\vec{n}$, can be defined everywhere on the external physical boundary, ∂V_{ext}, over different portions of which, ∂V_{ext}^- and ∂V_{ext}^+, the neutron angular flux, φ^{gk}, may be either *incoming* or *outgoing*, respectively, for a given discrete angular direction of flight, $\vec{\Omega}^k$; where $\partial V_{ext}^{\pm}:=\{\partial V_f:\vec{\Omega}^k\cdot\vec{n}\gtrless0,\forall\partial V_f\in\partial V_{ext}\}$. From their algebraic derivation, Morel and McGhee suggest that any

spurious solutions to the SAAF-S_N equation may be eliminated by requiring the neutron angular flux to satisfy the FONT-S_N equation over all outgoing portions of the physical boundary, ∂V_{ext}^{+}; q.v. Eq. (10d) [11].

Only Dirichlet-type incoming boundary conditions are considered in the above, $\partial V_{ext} := \partial V_V \cup \partial V_R$, where ∂V_V and ∂V_R denote the incoming portions of the boundary where vacuum and reflective boundaries conditions are prescribed, respectively; such that $\partial V_V^- := \partial V_V \cap \partial V_{ext}^-$ and $\partial V_R^- := \partial V_R \cap \partial V_{ext}^-$. One considers only those reflective boundaries that form a perpendicular plane with any of the axes in a rectangular Cartesian coordinate system, such that the specular reflection, $\vec{\Omega}^{k\prime}$, of each discrete ordinate, $\vec{\Omega}^k$, is also a member of the Level-Symmetric or Gauss–Chebyshev angular quadrature sets; where for $\varphi^{gk\prime} = \varphi^g(\vec{\Omega}^{k\prime})$, $\left|\vec{\Omega}^{k\prime} \cdot \vec{n}\right| = \left|\vec{\Omega}^k \cdot \vec{n}\right|$ and $w_{k\prime} = w_k$.

The defining equations can be recast in block-like group-ordinate operator notation:

$$L\varphi = Qq, \tag{11a}$$

$$= Q\left[S\varphi + F\varphi + \frac{1}{4\pi}q_x\right]; \tag{11b}$$

with the neutron angular flux, $\varphi = [\varphi^1, \ldots, \varphi^G]^T$, where $\varphi^g = [\varphi^{g1}, \ldots, \varphi^{gK}]^T$ for $g = 1, \ldots, G$; the strength of any extraneous fixed sources, $q_x = [q_x^1, \ldots, q_x^G]^T$; the diagonal-loss operator, L, comprises within-group losses due to streaming and total collision in each discrete ordinate, L^{gk}, Eq. (12a); the scatter operator, S, comprises potentially anisotropic group-to-group scatter terms in each discrete ordinate, S^{gk}, Eq. (12b); the fission operator, F, comprises isotropic group-to-group fission terms in each discrete ordinate, F^{gk}, Eq. (12c):

$$L^{gk}\varphi := -\vec{\Omega}^k \cdot \vec{\nabla}\frac{1}{\Sigma_t^g}\vec{\Omega}^k \cdot \vec{\nabla}\varphi^{gk} + \Sigma_t^g\varphi^{gk}; \tag{12a}$$

$$S^{gk}\varphi := \sum_{g\prime=1}^{G}\sum_{l=0}^{L}\sum_{m=-l}^{l}\Sigma_{sl}^{g\prime\to g}Y_l^m\boldsymbol{\Phi}_l^{g\prime m}; \tag{12b}$$

$$F^{gk}\varphi := \chi^g\sum_{g\prime=1}^{G}\nu^{g\prime}\Sigma_f^{g\prime}Y_0^0\boldsymbol{\Phi}_0^{g\prime 0}. \tag{12c}$$

For completeness, a Legendre polynomial (P_L) expansion of the scattering kernel has been included. However, within the scope of this paper, one is content in the limit of $L = 0$; likewise, only isotropic fission and extraneous fixed sources are considered. The multi-group components of the spherical harmonic flux moments, $\boldsymbol{\Phi}_l^{gm}$, are evaluated for $1, \ldots, G$:

$$\boldsymbol{\Phi}_l^{gm}(\vec{r}) \approx \sum_{k=1}^{K} w_k Y_l^m(\vec{\Omega}^k)\varphi^{gk}(\vec{r}). \tag{13}$$

The operator, Q, that acts group-ordinate-wise upon each of the source terms on the right-hand side of Eq. (11) is defined compactly as:

$$Q = 1 + X. \tag{14}$$

For the group-ordinate components of the operator X defined for $g = 1, \ldots, G$ and $k = 1, \ldots, K$:

$$X^{gk} := -\vec{\Omega}^k \cdot \vec{\nabla}\frac{1}{\Sigma_t^g}, \tag{15}$$

defining the operator, A, such that:

$$A\varphi = (L - QS)\varphi, \tag{16}$$

one can distinguish extraneous, or fixed, source problems where the source is independent of the neutron distribution:

$$(A - QF)\varphi = \frac{1}{4\pi}Qq_x, \tag{17}$$

from eigenvalue, or effective multiplication factor (k_{eff}), problems:

$$A\varphi = \frac{1}{k_{eff}}QF\varphi. \tag{18}$$

4. A SIP-DG-IGA spatial discretization

One seeks to approximate the (semi-)analytic solution by some finite linear combination of basis functions and expansion coefficients. Within a discontinuous framework, one exploits the broken Sobolev space, $H^s(\mathcal{T})$, which defines a set of spaces, $H^s(V_e)$, spanned by locally supported functions that belong to the regular Sobolev space, in the restriction to V_e:

$$H^s(\mathcal{T}) := \{u \in L_2(V) : u|_{V_e} \in H^s(V_e), \forall V_e \in \mathcal{T}(V)\}; \tag{19}$$

where the usual Sobolev embeddings rules apply; i.e. $H^{s+1}(\mathcal{T}) \subset H^s(\mathcal{T})$. The associated broken inner-product and broken norm, are given below in Eqs. (20a) and (20b), respectively:

$$(u,v)_{H^s(\mathcal{T})} := \sum_{V_e \in \mathcal{T}(V)} (u,v)_{H^s(V_e)}; \tag{20a}$$

$$\|u\|_{H^s(\mathcal{T})} := (u,u)^{1/2}_{H^s(\mathcal{T})}. \tag{20b}$$

The restriction of such functions with support over V_e are defined over ∂V_e by trace operators, $\gamma_i : H^s(V_e) \to H^{s-i-1/2}(\partial V_e)$ for $0 \le i < s$ [46]. Of particular interest is the Dirichlet trace, γ_0, which is well defined in $L_2(\partial V_e)$ for $s > 1/2$:

$$\gamma_0 u := u|_{\partial V_e}. \tag{21}$$

One notes that this condition is less strict than that imposed by a DG discretization of the NDE; consistency of its discretization would require $s > 3/2$ in order for the restriction of the normal components of the gradient of functions, or the Neumann trace, to be well defined over ∂V_e [28].

Any function $u \in H^s(\mathcal{T})$ is discontinuous across V, yet smooth enough within an element to admit two-valued traces at an interface for $s > 1/2$; with *jumps*, $[\![\cdot]\!]_{\partial V_f}$, and *averages*, $\{\{\cdot\}\}_{\partial V_f}$, defined for some scalar-valued function, u, in Eqs. (22a) and (22b), respectively:

$$[\![u]\!]_{\partial V_f} := \begin{cases} u^+ - u^-, & \forall \partial V_f \in \partial V_{int}; \\ u, & \forall \partial V_f \in \partial V_{ext}; \end{cases} \tag{22a}$$

$$\{\{u\}\}_{\partial V_f} := \begin{cases} \frac{1}{2}(u^+ + u^-), & \forall \partial V_f \in \partial V_{int}; \\ u, & \forall \partial V_f \in \partial V_{ext}. \end{cases} \tag{22b}$$

Although arbitrary, the definitions are perspective-dependent. The superscript (+) pertains to the *active*-element, V_+, whose outward-pointing normal vector over its boundary, $\vec{n}^+$, coincides with that, $\vec{n}$, at the interface, $V_+ \cap V_-$; whereas the superscript (−) pertains to the *neighbor*-element, V_-, whose outward-pointing normal vector over its boundary, $\vec{n}^-$, has the opposite orientation to that of the active-element; i.e. $\vec{n} = \vec{n}^+ = -\vec{n}^-$. To allow for compact notation, the jumps and averages over those boundaries that lie adjacent to the physical boundary, ∂V_{ext}, have also been included above.

Physically, the solution should be sufficiently smooth that any jumps in the angular flux, φ, and any jumps in the normal component of the neutron angular current, $\vec{\Omega}\varphi \cdot \vec{n}$, are negligibly small across the interior of the domain in the real physical space; i.e.:

$$\left.\begin{matrix} [\![\varphi]\!]_{\partial V_f}; \\ [\![\vec{\Omega}\varphi \cdot \vec{n}]\!]_{\partial V_f} \end{matrix}\right\} = 0, \quad \forall \partial V_f \in \partial V_{int}. \tag{23}$$

One formulates the weak form by multiplying Eq. (11) by test functions, $w \in \mathcal{V}(\mathcal{T})$, integrating over each V_e and then taking the sum of these contributions. The neutron angular flux is expanded in a basis of trial functions from the same space, $u \in \mathcal{V}(\mathcal{T}) \subseteq H^s(\mathcal{T})$, which is the s-order broken Sobolev space, Eq. (19). By application of the divergence theorem to each of the streaming terms, the basis functions are only required to be first-order differentiable; viz. $H^1(\mathcal{T})$ is an appropriate space.

The proposed spatial discretization is non-conforming since $\hat{\varphi} \in \mathcal{V}(\mathcal{T}) \not\subset \mathcal{V}(V) \ni \varphi$; and properties of the (semi-)analytical solution cannot be assumed by the discrete one. It will be necessary to establish directly discrete stability and consistency. The discrete variational problem is posed by restricting the collection of infinite spaces of basis functions to finite-dimensional subsets; i.e. $\hat{\mathcal{V}}_{h,p}(\mathcal{T}) \subset \mathcal{V}(\mathcal{T})$. As per the isoparametric concept, these broken spaces are chosen as those spanned by the same N_e-number of NURBS basis functions used to describe the patches, V_e. Although the basis may be smooth within a given patch, it is discontinuous across the boundaries. The NURBS basis functions, R, Eq. (3), are characterized by the mesh spacing, h, as well as the polynomial degree of the basis, p; i.e. $\forall V_e \in \mathcal{T}$:

$$\begin{cases} \left[\hat{\mathcal{V}}_{h,p}(V_e)\right]^T = \text{span}\left\{R_i^p\right\}_{i=1}^{N_e}, \\ \text{with } \text{supp}\left(R^p\right) = \left\{\vec{r} \in V_e : R_i^p(\vec{r}) \neq 0 \text{ for } i = 1, \ldots, N_e\right\}. \end{cases} \tag{24}$$

Indeed, the tensor-product structure of the parametric domain permits the NURBS basis functions to be constructed from different polynomials in different parametric directions; however, for simplicity, they are characterized by a single p and unless necessary, the superscript is suppressed.

Clearly, $\hat{\mathcal{V}}_{h,p}(\mathcal{T})$ is chosen such that $\hat{\varphi} \to \varphi$ as $N \to \infty$. The weighted-residual statement must be satisfied for each member in the weighting set; and since the space of trial and test functions coincide, this forms the same number of algebraic equations as there are unknowns per group; i.e. $DoF_e^{gk} = \dim \hat{\mathcal{V}}_{h,p}(V_e) = N_e$ and $DoF^{gk} = \sum_{V_e} DoF_e^{gk} = N$ for $k = 1, \ldots, K$; and hence, $DoF^g = \sum_k DoF^{gk} = K \times N$ for $g = 1, \ldots, G$; and hence, $DoF = \sum_g DoF^g = G \times K \times N$. Consequently, for the analysis over a single energy-independent mesh, the discrete problem is posed as a system of $(GKN \times GKN)$-matrix equations.

The weak form naturally satisfies the vacuum boundary condition over the inflow portions of the exterior boundary, ∂V_{ext}^{-}; q.v. Eq. (10b). The reflective boundary condition is implemented by substitution of Eq. (10c). Boundary conditions must also be prescribed over those outflow portions ∂V_{ext}^{+}, where the solution must satisfy the FONT-S_N equation; q.v. Eq. (10d). Equally, this condition is required to hold over those faces to the interior of the mesh, ∂V_{int}.

As it stands, the discrete variational statement of Eq. (17) is to find $\hat{\varphi} \in \hat{\mathcal{V}}_{h,p}(\mathcal{T})$, such that:

$$a(\hat{\varphi}, \hat{w}) = b(\hat{w}), \quad \forall\, \hat{w} \in \hat{\mathcal{V}}_{h,p}(\mathcal{T}). \tag{25}$$

The discrete bilinear form, $a(\cdot,\cdot) : \hat{\mathcal{V}}_{h,p}(\mathcal{T}) \times \hat{\mathcal{V}}_{h,p}(\mathcal{T}) \to \mathbb{R}$, has block-like structure and comprises terms of streaming and total collision, group-to-group scattering and fission, leakage across the union of interfaces and outflow portions of the external boundary, $\partial V_{IP} = (\partial V_{ext}^{-})^{c} = \partial V_{int} \cup \partial V_{ext}^{+}$, and the weak enforcement of incoming boundary conditions over ∂V_{ext}^{-}:

$$a(\hat{\varphi}, \hat{w}) = a_L(\hat{\varphi}, \hat{w}) - a_S(\hat{\varphi}, \hat{w}) - a_F(\hat{\varphi}, \hat{w}) + a_{IP}(\hat{\varphi}, \hat{w}) + a_{ext}(\hat{\varphi}, \hat{w}). \tag{26}$$

In turn, each of these is defined below, respectively, suppressing any spatial dependence:

$$\begin{aligned} a_L(\hat{\varphi}, \hat{w}) &= \sum_{g=1}^{G}\sum_{k=1}^{K} w_k \left[\sum_{V_e \in \mathcal{T}} \int_{V_e} \vec{\Omega}^k \cdot \vec{\nabla} \hat{w} \frac{1}{\Sigma_{t,e}^{g}} \vec{\Omega}^k \cdot \vec{\nabla} \hat{\varphi}^{gk} + \hat{w} \Sigma_{t,e}^{g} \hat{\varphi}^{gk} \, dV \right], \\ &= \sum_{g=1}^{G}\sum_{k=1}^{K} a_L^{gk}(\hat{\varphi}^{gk}, \hat{w}); \end{aligned} \tag{27a}$$

$$\begin{aligned} a_S(\hat{\varphi}, \hat{w}) &= \sum_{g=1}^{G}\sum_{k=1}^{K} w_k \left[\sum_{g'=1}^{G} Y_0^0(\vec{\Omega}^k) \sum_{V_e \in \mathcal{T}} \int_{V_e} \hat{w} \Sigma_{s0,e}^{g' \to g} \hat{\boldsymbol{\Phi}}_0^{g'0} + \vec{\Omega}^k \cdot \vec{\nabla} \hat{w} \frac{\Sigma_{s0,e}^{g' \to g}}{\Sigma_{t,e}^{g}} \hat{\boldsymbol{\Phi}}_0^{g'0} \, dV \right], \\ &= \sum_{g=1}^{G}\sum_{k=1}^{K} a_S^{gk}(\hat{\varphi}, \hat{w}); \end{aligned} \tag{27b}$$

$$\begin{aligned} a_F(\hat{\varphi}, \hat{w}) &= \sum_{g=1}^{G}\sum_{k=1}^{K} w_k \left[\sum_{g'=1}^{G} Y_0^0(\vec{\Omega}^k) \sum_{V_e \in \mathcal{T}} \chi_e^{g} \int_{V_e} \hat{w} \nu_e^{g'} \Sigma_{f,e}^{g'} \hat{\boldsymbol{\Phi}}_0^{g'0} + \vec{\Omega}^k \cdot \vec{\nabla} \hat{w} \frac{\nu_e^{g'} \Sigma_{f,e}^{g'}}{\Sigma_{t,e}^{g}} \hat{\boldsymbol{\Phi}}_0^{g'0} \, dV \right], \\ &= \sum_{g=1}^{G}\sum_{k=1}^{K} a_F^{gk}(\hat{\varphi}, \hat{w}); \end{aligned} \tag{27c}$$

$$\begin{aligned} a_{IP}(\hat{\varphi}, \hat{w}) &= \sum_{g=1}^{G}\sum_{k=1}^{K} w_k \left[\sum_{V_e \in \mathcal{T}} \sum_{\partial V_f \in V_e \cap \partial V_{IP}} \int_{\partial V_f} \hat{w} \vec{\Omega}^k \hat{\varphi}^{gk} \cdot \vec{n} \, dS \right], \\ &= \sum_{g=1}^{G}\sum_{k=1}^{K} w_k \left[\sum_{\partial V_f \in \partial V_{IP}} \int_{\partial V_f} [\![\hat{w} \vec{\Omega}^k \hat{\varphi}^{gk} \cdot \vec{n}]\!] \, dS \right], \\ &= \sum_{g=1}^{G}\sum_{k=1}^{K} a_{IP}^{gk}(\hat{\varphi}^{gk}, \hat{w}); \end{aligned} \tag{27d}$$

$$\begin{aligned} a_{ext}(\hat{\varphi}, \hat{w}) &= \sum_{g=1}^{G}\sum_{k=1}^{K} w_k \left[\sum_{V_e \in \mathcal{T}} \sum_{\partial V_f \in V_e \cap \partial V_R^{-}} - \int_{\partial V_f} \left| \vec{\Omega}^k \cdot \vec{n} \right| \hat{w} \hat{\varphi}^{gk\prime} \, dS \right], \\ &= \sum_{g=1}^{G}\sum_{k=1}^{K} a_{ext}^{gk}(\hat{\varphi}^{g}, \hat{w}). \end{aligned} \tag{27e}$$

The discrete linear functional, $b(\cdot) : \hat{\mathcal{V}}_{h,p}(\mathcal{T}) \to \mathbb{R}$, comprises only fixed sources:

$$\begin{aligned} b(\hat{w}) &= \sum_{g=1}^{G}\sum_{k=1}^{K} w_k \left[\sum_{V_e \in \mathcal{T}} \int_{V_e} \hat{w} \frac{1}{4\pi} q_{x,e}^{g} + \vec{\Omega}^k \cdot \vec{\nabla} \hat{w} \frac{1}{4\pi \Sigma_{t,e}^{g}} q_{x,e}^{g} \, dV \right], \\ &= \sum_{g=1}^{G}\sum_{k=1}^{K} b^{gk}(\hat{w}). \end{aligned} \tag{28}$$

For multiplying systems, $q_x = 0$, the weak form of Eq. (18) is to find $\hat{\varphi} \in \hat{\mathcal{V}}_{h,p}(\mathcal{T})$, such that:

$$\tilde{a}(\hat{\varphi}, \hat{w}) = \frac{1}{\mathrm{k_{eff}}} a_f(\hat{\varphi}, \hat{w}), \quad \forall\, \hat{w} \in \hat{\mathcal{V}}_{h,p}(\mathcal{T}); \tag{29}$$

where $\tilde{a}$ is the original bilinear form in Eq. (26), a, less the fission term; i.e.:

$$\tilde{a} = a + a_F = a_L - a_S + a_{IP} + a_{ext}. \tag{30}$$

The properties of neutron conservation and symmetry are preserved in developing an interior penalty scheme for the discretized bilinear form.

Consistency. The discretization is consistent if the true solution satisfies the discrete system of equations. However, one cannot simply substitute φ into Eq. (25) because the bilinear form, a, has been defined on $\hat{\mathcal{V}}_{h,p}(\mathcal{T})\times\hat{\mathcal{V}}_{h,p}(\mathcal{T})$; and similarly for $\tilde{a}$ in Eq. (29). Therefore, one must assume that $\varphi\in\mathcal{V}^*(V)\subset\mathcal{V}(V)$; and second, that $\hat{\varphi}^*\in\hat{\mathcal{V}}^*_{h,p}(\mathcal{T})=\mathcal{V}^*(V)+\hat{\mathcal{V}}_{h,p}(\mathcal{T})$; such that the bilinear form can be extended to be bounded on $\hat{\mathcal{V}}_{h,p}(\mathcal{T})\times\hat{\mathcal{V}}^*_{hp}(\mathcal{T})$. The space $\hat{\mathcal{V}}^*_{h,p}(\mathcal{T})$ is equipped with the norm $\|\cdot\|_{\hat{\epsilon}^*}$, such that for some arbitrary function, u, and some constant C:

$$\|u\|_{\hat{\epsilon}^*}=\|u\|_{\hat{\epsilon}}\,,\qquad\forall u\in\hat{\mathcal{V}}_{h,p}(\mathcal{T});\tag{31a}$$

$$\|u\|_{\hat{\epsilon}^*}<C\,\|u\|_{\epsilon^*}\,,\qquad\forall u\in\mathcal{V}^*(V).\tag{31b}$$

The former implies an equivalence of the norms $\|\cdot\|_{\hat{\epsilon}^*}$ and $\|\cdot\|_{\hat{\epsilon}}$ on $\hat{\mathcal{V}}_{h,p}(\mathcal{T})$; and the latter implies that $\mathcal{V}^*(V)\subset\hat{\mathcal{V}}^*_{h,p}(\mathcal{T})$; where $\|\cdot\|_{\hat{\epsilon}}$ and $\|\cdot\|_{\epsilon^*}$ are the energy-norms associated with the discrete bilinear form, $\hat{\mathcal{V}}_{h,p}(\mathcal{T})\times\hat{\mathcal{V}}_{h,p}(\mathcal{T})$, and the analytical one, $\mathcal{V}^*(V)\times\mathcal{V}^*(V)$, respectively.

From the definition of jumps, Eq. (22a), the first line of Eq. (27d) expressed as a sum of integrals over element boundaries can be re-expressed in the second line as a sum of integrals over interfaces and outflow portions of the external boundary, which can then be developed further using the definition of averages, Eq. (22b); i.e. suppressing the spatial dependence for $g=1,\dots,G$ and for $k=1,\dots,K$:

$$\begin{aligned}&\sum_{\partial V_f\in\partial V_{IP}}\int_{\partial V_f}[\![\hat{w}\vec{\Omega}^k\hat{\varphi}^{gk*}\cdot\vec{n}]\!]\,dS\\&=\sum_{\partial V_f\in\partial V_{int}}\int_{\partial V_f}[\![\hat{w}\vec{\Omega}^k\hat{\varphi}^{gk*}\cdot\vec{n}]\!]\,dS+\sum_{V_e\in\mathcal{T}}\sum_{\partial V_f\in V_e\cap\partial V^+_{ext}}\int_{\partial V_f}\hat{w}\vec{\Omega}^k\hat{\varphi}^{gk*}\cdot\vec{n}\,dS,\end{aligned}\tag{32a}$$

$$=\sum_{\partial V_f\in\partial V_{int}}\int_{\partial V_f}\{\{\hat{w}\}\}\underbrace{[\![\vec{\Omega}^k\hat{\varphi}^{gk*}\cdot\vec{n}]\!]}_{0}\,dS+\sum_{\partial V_f\in\partial V_{IP}}\int_{\partial V_f}[\![\hat{w}]\!]\{\{\vec{\Omega}^k\hat{\varphi}^{gk*}\cdot\vec{n}\}\}\,dS.\tag{32b}$$

The strong form, including the boundary conditions, Eqs. (10), are retrieved by substitution of φ into the discrete weak-problem, Eq. (25); and by application of the divergence theorem to the first term in Eq. (27a), the double-differential term is recouped. This is followed by the re-expression of a_{IP}, Eq. (27d), in terms of Eq. (32b); and then accounting for the regularity in the true solution, Eqs. (23). Thus, the discrete problem is consistent provided that the numerical fluxes are consistent; and exploiting continuity of the normal component of $\vec{\Omega}^k$ across interfaces, the following modification can be made for $g=1,\dots,G$ and for $k=1,\dots,K$:

$$\Longrightarrow a^{gk}_{IP}(\hat{\varphi}^{gk*},\hat{w})=\sum_{\partial V_f\in\partial V_{IP}}\int_{\partial V_f}\vec{\Omega}^k\cdot\vec{n}[\![\hat{w}]\!]\{\{\hat{\varphi}^{gk*}\}\}\,dS.\tag{33}$$

Galerkin's property of orthogonality stems from consistency such that the error in the numerical solution is orthogonal to the chosen subspace since $\mathcal{V}^*(V)\subset\hat{\mathcal{V}}^*_{h,p}(\mathcal{T})$. A strong definition of consistency has been enforced; yet, since Legendre–Gauss quadrature rules are employed to evaluate all integral quantities, one can expect the discretization to be consistent asymptotically.

The general rule of p+1 quadrature points may not be sufficient to evaluate the boundary integrals because the integrands are polynomial constructs of a combined maximal polynomial degree of $p+p-1+p=3p-1$; q.v. Eq. (33). Where each component of the normal vector, $\vec{n}$, is itself a linear combination of derivatives of the same functions; viz. polynomial constructs of degree $p-1$. Using Legendre–Gauss quadrature rules, the boundary integral should be evaluated with a sufficient number of quadrature points, N_q, in each of the $(d-1)$-directions over the canonical representation of the boundary in the parent space; i.e. for $p>1$:

$$2N_q-1\;\geq\;3p-1;\tag{34a}$$

$$\Longrightarrow N_q\;=\;\begin{cases}\dfrac{3p}{2}, & \text{for } p\text{-even};\\[2ex]\dfrac{3p+1}{2}, & \text{for } p\text{-odd}.\end{cases}\tag{34b}$$

Symmetry. It is desirable to retain the property of symmetry in the discrete bilinear form; e.g. to employ the well-established conjugate gradient (CG) method for sparse symmetric positive-definite (SPD) matrices. Therefore, the following is appended to a_{IP} for $g=1,\dots,G$ and for $k=1,\dots,K$:

$$\sum_{\partial V_f\in\partial V_{int}}\theta\int_{\partial V_f}\vec{\Omega}^k\cdot\vec{n}\{\{\hat{w}\}\}[\![\hat{\varphi}^{gk*}]\!]\,dS=0,\quad\forall\partial V_f\in\partial V_{int};\tag{35}$$

or rather redundantly, symmetry is reclaimed by letting $\theta=1$ in the following modification to a^{gk}_{IP}, Eq. (33), for $g=1,\dots,G$ and for $k=1,\dots,K$:

$$\implies a^{gk}_{IP}(\hat{\varphi}^{gk*}, \hat{w}) = a^{gk}_{IP_c}(\hat{\varphi}^{gk*}, \hat{w}) + a^{gk}_{IP_s}(\hat{\varphi}^{gk*}, \hat{w}), \tag{36a}$$

$$\begin{aligned} &= \sum_{\partial V_f \in \partial V_{IP}} \int_{\partial V_f} \vec{\Omega}^k \cdot \vec{n} [\![\hat{w}]\!] \{\{\hat{\varphi}^{gk*}\}\} \, dS \\ &+ \sum_{\partial V_f \in \partial V_{int}} \theta \int_{\partial V_f} \vec{\Omega}^k \cdot \vec{n} \{\{\hat{w}\}\} [\![\hat{\varphi}^{gk*}]\!] \, dS. \end{aligned} \tag{36b}$$

Consistency is maintained as $[\![\varphi]\!] = 0$ across the interior of the domain.

With the exception of a_{IP}, Eqs. (27) are given as a sum over elements or boundaries whose local contributions are the product of basis functions with local support over the same domain. Differently, Eq. (36) comprises a sum over interfaces, whose local contributions are the product of basis functions that may not necessarily have local support over the same element, such that a_{IP} can be block-partitioned. Computationally, savings can be made by considering that the symmetry-part of the block is simply the transpose of the consistency-part [28].

Penalty. As per the Lax–Milgram Lemma, the properties of continuity and coercivity are sufficient conditions to assert well-posedness [47].

For $\hat{u} \in \hat{\mathcal{V}}^*_{h,p}(\mathcal{T})$ and $\hat{v} \in \hat{\mathcal{V}}_{h,p}(\mathcal{T})$ and some constant, $C_\alpha > 0$, the discrete bilinear form is bounded on $\hat{\mathcal{V}}_{h,p}(\mathcal{T}) \times \hat{\mathcal{V}}^*_{hp}(\mathcal{T})$ if:

$$a(\hat{u}, \hat{v}) \leq C_\alpha \, \|\hat{v}\|_{\hat{\epsilon}} \, \|\hat{u}\|_{\hat{\epsilon}^*} \, ; \tag{37}$$

and for $\hat{u} \in \hat{\mathcal{V}}_{h,p}(\mathcal{T})$ and some constant, $C_\beta > 0$, the discrete bilinear form is coercive if:

$$a(\hat{u}, \hat{u}) \geq C_\beta \, \|u\|^2_{\hat{\epsilon}} \, . \tag{38}$$

The latter is often simply guaranteed by the nature of the problem; however, owing to the arbitrariness of the normal vector over an interface, the sign-indefinite consistency and the symmetry terms in Eq. (36) are potentially negative terms. In general, it is not possible to uphold a statement of coercivity without some (residual-based) stabilization mechanism [48].

Discontinuities in the numerical approximation result from the non-conformity in seeking a discrete solution in a broken function space. A final modification is thus made to a_{IP}, such that appended to the bilinear form is a residual-dependent term that *contributes* to the coercivity by penalizing the error, or rather quashing any jumps, $[\![\vec{\Omega}\hat{\varphi} \cdot \vec{n}]\!]$, across the set of discontinuous patch interfaces. Stability of the discretization is enhanced and invertibility is ensured under refinement for some suitable selection of penalty parameters, $\mu^g_f > 0$, for $g = 1, \ldots, G$ and for $k = 1, \ldots, K$:

$$\begin{aligned} \implies a^{gk}_{IP}(\hat{\varphi}^{gk*}, \hat{w}) = &\sum_{\partial V_f \in \partial V^+_{ext}} \int_{\partial V_f} \hat{w} \vec{\Omega}^k \hat{\varphi}^{gk*} \cdot \vec{n} \, dS \\ &+ \sum_{\partial V_f \in \partial V_{int}} \int_{\partial V_f} \vec{\Omega}^k \cdot \vec{n} [\![\hat{w}]\!] \{\{\hat{\varphi}^{gk*}\}\} \, dS + \theta \int_{\partial V_f} \vec{\Omega}^k \cdot \vec{n} \{\{\hat{w}\}\} [\![\hat{\varphi}^{gk*}]\!] \, dS \\ &+ \sum_{\partial V_f \in \partial V_{int}} \mu^g_f \int_{\partial V_f} [\![\vec{\Omega}^k \hat{w} \cdot \vec{n}]\!] [\![\vec{\Omega}^k \hat{\varphi}^{gk*} \cdot \vec{n}]\!] \, dS. \end{aligned} \tag{39}$$

Choosing numerical fluxes that connect the elements through their interfaces as per an interior penalty scheme provides a *good* compromise of sparsity and conditioning of the ensuing matrix equations [49]. Whilst the latter is dependent upon the *tuning* of the penalty parameters, the former is better understood from a perspective of implementation. Owing to the local formulation, the elementary stencil for the proposed IP-DG discretization accounts for those volume contributions over elements as well as those face contributions over interfaces formed with *direct* neighbors that share a face; viz. as per the tensor-product structure of the parametric space, the elementary stencil contains at most $(1+d^2)$-elements.

The particular choice to penalize the neutron angular current will ease the derivation of the penalty parameters in Section 4.1. Since Dirichlet boundary conditions are satisfied *naturally*, they do not need to be enforced by penalization. Again, the properties of symmetry, for $\theta = 1$, and consistency have been maintained; and error bounds can be established as per Strang's Second Lemma of quasi-best approximation for non-conforming and consistent discretizations [28,50].

Weakly coupled in energy and angle, the within-group equations can be solved sequentially using the most up-to-date information. In the presence of extraneous fixed-sources, $\hat{\varphi}^{gk} \in \hat{\mathcal{V}}_{h,p}(\mathcal{T})$ is solved for $g = 1, \ldots, G$ and for $k = 1, \ldots, K$:

$$a^{gk}_L(\hat{\varphi}^{gk}, \hat{w}) + a^{gk}_{IP}(\hat{\varphi}^{gk}, \hat{w}) = a^{gk}_S(\hat{\varphi}, \hat{w}) + a^{gk}_F(\hat{\varphi}, \hat{w}) - a^{gk}_{ext}(\hat{\varphi}^{gk}, \hat{w}) + b^{gk}(\hat{w}), \quad \forall \, \hat{w} \in \hat{\mathcal{V}}_{h,p}(\mathcal{T}). \tag{40}$$

Since the left-hand side, $a^{gk}_L + a^{gk}_{IP}$, is SPD for $\theta = 1$, one can employ efficient iterative smoothers, such as the pre-conditioned conjugate gradient (PCG) method. Additional savings can be made for the storage of symmetric matrices.

The eigenvalue problem is cast as finding $\hat{\varphi}^{gk} \in \hat{\mathcal{V}}_{h,p}(\mathcal{T})$ for $g = 1, \ldots, G$ and for $k = 1, \ldots, K$:

$$a^{gk}_L(\hat{\varphi}^{gk}, \hat{w}) + a^{gk}_{IP}(\hat{\varphi}^{gk}, \hat{w}) = a^{gk}_S(\hat{\varphi}, \hat{w}) + \frac{1}{\mathrm{k_{eff}}} a^{gk}_F(\hat{\varphi}, \hat{w}) - a^{gk}_{ext}(\hat{\varphi}^{gk}, \hat{w}), \quad \forall \, \hat{w} \in \hat{\mathcal{V}}_{h,p}(\mathcal{T}). \tag{41}$$

For eigenvalue problems, one normalizes the solution after each outer-iteration such that $a_F(\hat{\phi}, \hat{\phi}) = 1$.

4.1. A discrete coercivity analysis

There exist myriad interior penalty schemes, each proposing its own combination of numerical fluxes and stabilization mechanisms [48,49]. Limiting the scope somewhat, the three standard variations, the non-symmetric interior penalty (NIP), the incomplete interior penalty (IIP) and the symmetric interior penalty (SIP) schemes can be expressed by setting θ to -1, 0 and 1, respectively, in Eq. (39). The NIP-DG scheme is coercive for any choice of $\mu_f > 0$; whereas a lower bound must be imposed on the IIP and the SIP variations. For reasons already discussed, only the latter is investigated; yet, for completeness, the variable θ is retained.

The performance of the SIP-DG discretization depends heavily upon the choice of penalty parameters; without being arbitrarily so, they must be large enough to ensure definiteness and invertibility of the matrix equations. Therefore, one aims to establish a lower bound for the penalty parameters through a coercivity analysis of the bilinear form, based upon the methodology presented by Shahbazi [51].

Since the discretized system is only weakly coupled in energy and angle, it is sufficient to consider separately the coercivity of each group-ordinate bilinear form, the left-hand side of Eqs. (40) and (41); where $a^{gk}_{lhs}(\hat{u},\hat{u})$ is recalled below for some $\hat{u} \in \hat{\mathcal{V}}_{h,p}(\mathcal{T})$, suppressing the spatial dependence for $g = 1,\dots,G$ and for $k = 1,\dots,K$:

$$a^{gk}_{lhs}(\hat{u},\hat{u}) = a^{gk}_{L}(\hat{u},\hat{u}) + a^{gk}_{IP}(\hat{u},\hat{u}), \tag{42a}$$

$$\begin{aligned} &= \sum_{V_e\in\mathcal{T}} \int_{V_e} \frac{1}{\Sigma^g_{t,e}} (\vec{\Omega}^k\cdot\vec{\nabla}\hat{u})^2 + \Sigma^g_{t,e}(\hat{u})^2 \, dV + \sum_{\partial V_f\in\partial V^+_{ext}} \int_{\partial V_f} \left|\vec{\Omega}^k\cdot\vec{n}\right| (\hat{u})^2 \, dS \\ &+ \sum_{\partial V_f\in\partial V_{int}} (1+\theta) \int_{\partial V_f} [\![\vec{\Omega}^k\hat{u}\cdot\vec{n}]\!]\{\{\hat{u}\}\} \, dS + \sum_{\partial V_f\in\partial V_{int}} \mu^g_f \int_{\partial V_f} ([\![\vec{\Omega}^k\hat{u}\cdot\vec{n}]\!])^2 \, dS. \end{aligned} \tag{42b}$$

As per the arbitrariness of the normal vector defined over an interface, the only potentially negative term and thus, the only one that may not *contribute* towards the coercivity is that in the second line of Eq. (42b).

Rather pessimistically, and regardless of the actual direction of neutron travel, $\vec{\Omega}^k$, every element face to the interior of the mesh, $\partial V_f \in \partial V_{int}$, is treated as an inflow boundary, $\vec{\Omega}^k\cdot\vec{n} < 0$; and thus, the first term of the second line of Eq. (42b) is assumed to be negative. This may lead to an over-penalization of certain interfaces of a given discrete group-ordinate bilinear forms. However, it does yield penalty parameters that depend only upon multi-group cross-section data; and they can be calculated in a pre-processing step. Future research may investigate group-ordinate-dependent penalty parameters; however, this would require significantly more computational storage.

Sufficient penalization of each face $\partial V_f \in \partial V_{IP}$, ensures coercivity of the bilinear form with respect to the energy-norm, which is defined for some $\hat{u} \in \hat{\mathcal{V}}_{h,p}(\mathcal{T})$ and for $g = 1,\dots,G$ and for $k = 1,\dots,K$:

$$\begin{aligned} \|\hat{u}\|^2_{\hat{e}gk} &:= \sum_{V_e\in\mathcal{T}} \int_{V_e} \frac{1}{\Sigma^g_{t,e}} (\vec{\Omega}^k\cdot\vec{\nabla}\hat{u})^2 + \Sigma^g_{t,e}(\hat{u})^2 \, dV + \sum_{\partial V_f\in\partial V^+_{ext}} \int_{\partial V_f} \left|\vec{\Omega}^k\cdot\vec{n}\right| (\hat{u})^2 \, dS \\ &+ \sum_{\partial V_f\in\partial V_{int}} \mu^g_f \int_{\partial V_f} ([\![\vec{\Omega}^k\hat{u}\cdot\vec{n}]\!])^2 \, dS. \end{aligned} \tag{43}$$

From the definition of jumps, Eq. (22a), and averages, Eq. (22b); and letting $a = [\![\vec{\Omega}^k\hat{u}\cdot\vec{n}]\!]$ and $b = \{\{\hat{u}\}\}$ in Young's inequality for the product of two scalars:

$$ab \le \frac{\epsilon a^2}{2} + \frac{b^2}{2\epsilon}, \quad \forall\epsilon > 0. \tag{44}$$

and the substitution thereof into Eq. (42b) bounds the potentially negative term in the second line over all discontinuous faces, $\forall\partial V_f \in \partial V_{int}$; and collecting like-terms for $g = 1,\dots,G$ and for $k = 1,\dots,K$:

$$\begin{aligned} a^{gk}_{lhs}(\hat{u},\hat{u}) \ge a^{gk}_{L}(\hat{u},\hat{u}) &+ \sum_{\partial V_f\in\partial V^+_{ext}} \int_{\partial V_f} \left|\vec{\Omega}^k\cdot\vec{n}\right| (\hat{u})^2 \, dS \\ &- \sum_{\partial V_f\in\partial V_{int}} \frac{(1+\theta)}{2\epsilon_f} \int_{\partial V_f} (\{\{\hat{u}\}\})^2 \, dS \\ &+ \sum_{\partial V_f\in\partial V_{int}} \left(\mu^g_f - \frac{(1+\theta)\epsilon_f}{2}\right) \int_{\partial V_f} ([\![\vec{\Omega}^k\hat{u}\cdot\vec{n}]\!])^2 \, dS. \end{aligned} \tag{45}$$

By the definition provided in Eq. (22b), the term $(\{\{\hat{u}\}\})^2$ is expanded out, to which Eq. (44) is applied with $\epsilon = 1$; i.e. $a^2+b^2+2ab \le 2a^2 + 2b^2$. The result is rewritten as a sum of integrals over patch boundaries, where individual terms are collected onto their

respective patches; i.e.:

$$\begin{aligned} a_{lhs}^{gk}(\hat{u},\hat{u}) \geq a_{L}^{gk}(\hat{u},\hat{u}) &+ \sum_{\partial V_f \in \partial V_{ext}^{+}} \int_{\partial V_f} \left|\vec{\Omega}^k \cdot \vec{n}\right| (\hat{u})^2 \, dS \\ &- \sum_{V_e \in \mathcal{T}} (1+\theta) \left[\sum_{\partial V_f \in V_e \cap \partial V_{int}} \frac{1}{4\epsilon_f} \int_{\partial V_f} (\hat{u})^2 \, dS \right] \\ &+ \sum_{\partial V_f \in \partial V_{int}} \left(\mu_f^g - \frac{(1+\theta)\epsilon_f}{2} \right) \int_{\partial V_f} ([\![\vec{\Omega}^k \hat{u} \cdot \vec{n}]\!])^2 \, dS. \end{aligned} \tag{46}$$

Taking advantage of the equivalence of norms in the chosen function space, there exists a discrete trace inequality that bounds from above, up to some constant, the integral quantity of the restriction of a function, as defined over the boundary ∂V_e; i.e. for some function $\hat{u} \in \hat{\mathcal{V}}_{h,p}(V_e)$:

$$\left\| \gamma_0 \hat{u} \right\|_{L_2(\partial V_e)}^2 \leq C_{e,f}^0 \left\| \hat{u} \right\|_{L_2(V_e)}^2; \tag{47}$$

where $C_{e,f}^0$ is the trace inequality constant (TIC) that pertains to the Dirichlet trace in Eq. (21), for which those integrals over patch boundaries in second line of Eq. (46) are substituted; and one seeks the sharpest TIC values in order to optimize the penalty parameters. Following the developments made by Owens et al. the TICs can be calculated as generalized eigenvalue problems, agnostic of the underlying element type [41]. Wilson et al. calculated TICs in such a manner to optimize penalty parameters for a SIP-DG-IGA discretization of the multi-group NDE; however, in that instance, the trace inequality employed was for that of the Neumann trace [28].

Collecting like-terms and comparing against Eq. (38), the following conditions must be satisfied for $g = 1, \ldots, G$ and for $k = 1, \ldots, K$:

$$1 - (1+\theta) \left[\sum_{\partial V_f \in V_e \cap \partial V_{int}} \frac{C_{e,f}^0}{4 \Sigma_{t,e}^g \epsilon_f} \right] > 0, \qquad \forall V_e \in \mathcal{T}^g(V); \tag{48a}$$

$$\mu_f^g - \frac{(1+\theta)\epsilon_f}{2} > 0, \qquad \forall \partial V_f \in \partial V_{int}; \tag{48b}$$

One must choose $\epsilon_f > 0$, such that Eq. (48a) is satisfied over each element. This is achieved by separately bounding from below each term in the sum over the F_e-number of faces of a given element; and to ensure that Eqs. (48) hold, the maximum penalization is applied across an interface [52]. Encapsulated below, the group-dependent penalty parameters may be calculated in a pre-processing step for $g = 1, \ldots, G$:

$$\mu_f^g > \frac{1}{8}(1+\theta)^2 \max_{V_e \in \bigcap_{e\prime} V_{e\prime} \ni \partial V_f} \frac{C_{e,f}^0 F_e}{\Sigma_{t,e}^g}, \quad \forall \partial V_f \in \partial V_{int}. \tag{49a}$$

4.2. The Trace Inequality Constants (TICs)

The coercivity analysis reveals that the penalty parameters, μ_f, are proportional to a constant, $C_{e,f}^0$, from an inequality that bounds from above the Dirichlet trace of a function; q.v. Eq. (47). The problem of optimizing penalty parameters becomes one of minimizing these trace inequality constants (TICs); and one seeks the maximum eigenvalue, which corresponds to the provably sharp TIC in Eq. (47); i.e. $C_{e,f}^0 = \max_i \lambda_i$ [41]. Rewritten in matrix notation, both matrices from Eq. (47), mass matrices, form a regular pair; and so, they do not need to be orthogonalized.

In their SIP-DG-IGA spatial discretization of the multi-group NDE, the penalty parameters were proportional to a constant from the Neumann trace inequality and Wilson et al. had to orthogonalize the pair of symmetric positive semi-definite (SPSD) stiffness matrices before solving the generalized eigenvalue problem [28]. Explicit orthogonalization becomes increasingly computationally expensive for matrices of increasingly large dimension; e.g. for NURBS patches with a complex internal structure due to KI-1-refinement, $N_e \gg \mathcal{O}(10^1)$.

Moreover, since the current spatial discretization employs mass matrices in the generalized eigenvalue problem, one is not restricted to non-degenerate geometries where the derivatives of the volumetric NURBS basis functions must be square-integrable at the boundary [28]. For example, it is possible to calculate the TICs, and thus, the penalty parameters, for each side of a circle constructed from a single bi-quadratic NURBS patch, mapped from a tensor-product parametric space [28].

At the time of writing, only standard pre-conditioners and algebraic multi-grid methods were considered. However, the authors are aware of research into subspace correction pre-conditioners for DG discretizations of elliptic problems using a basis of Gauss–Lobatto functions [53]. This would allow for (S)IP schemes using arbitrarily large penalty parameters and polynomial degrees to be solved efficiently [53]. Subsequent research should investigate whether such pre-conditioners are also effective for higher-order NURBS-based discretizations.

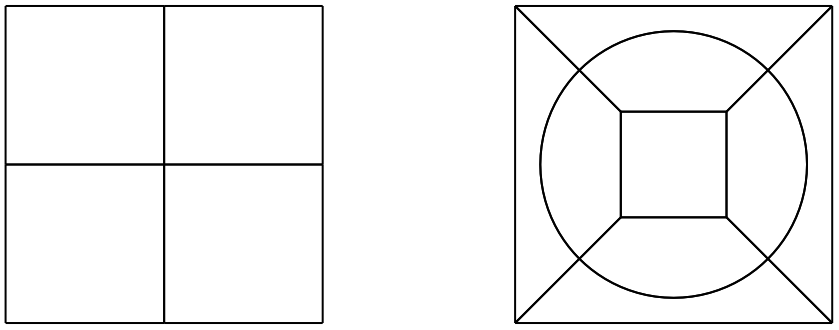

Fig. 1. The coarsest meshes of the MMS verification test cases defined over $V = [0,1]^2$: a Cartesian mesh (left) composed of four equal-volume bilinear NURBS patches; and a nuclear fuel pin-cell mesh (right) composed of *nine* equal-volume non-degenerate bi-quadratic NURBS patches.

5. The numerical results

This section presents some numerical results for the SIP-DG-IGA spatial discretization of the multi-group SAAF-S_N equation under uniform refinement. The method of manufactured solutions (MMS) is used to compare observed numerical convergence rates against optimal, theoretical ones. Then a series of nuclear reactor physics benchmark verification test cases are used to analyze the numerical accuracy of the proposed spatial discretization. Any data-plots that make reference to the DoFs of the discretized system account for all unknowns that were solved for in the complete system; viz. $DoF = G \times K \times N$ for G-number of groups and K-number of ordinates solved over an energy-independent mesh of N-number of control-variables.

The SIP-DG-IGA spatial discretization developed here has been implemented in a new, *modern* Fortran code [54]. The code adopts a distributed-memory computing software architecture using the Open MPI message passing. The code makes use of PETSc libraries; more specifically, its parallelization of linear matrix solution algorithms and its compressed row storage (CRS) for large, sparse-matrix data structures [55].

All *jobs* were submitted to the general purpose Imperial College high-performance computing (HPC) cluster computing service (CX1). The within-group within-angle matrix equations are converged to a tolerance of 1.00E−06 using PETSc's conjugate gradient (CG) iterative smoother, pre-conditioned by the BoomerAMG algebraic multi-grid method from the HYPRE library [56]. The neutron scalar flux is converged to a tolerance of 1.00E–06 between successive source iterations; and the eigenvalue is converged to a tolerance of 1.00E−08 between successive *power* iterations.

5.1. The Method of Manufactured Solutions (MMS)

The method of manufactured solutions (MMS) is used to investigate the proposed SIP-DG-IGA spatial discretization of the multi-group SAAF-S_N equation; cf. an overview by Salari et al. [57]. A smooth manufactured solution is chosen to test against theoretical orders of accuracy [58,59]:

$$|e|_{H^1} \leq C_1 h^{\min\{p,r\}}; \tag{50a}$$

$$\|e\|_{L_2} \leq C_2 h^{\min\{p+1,r\}}; \tag{50b}$$

where $e = \phi - \hat{\phi}$ is the discretization error; h is the characteristic mesh-spacing, p is the polynomial degree of the underlying NURBS basis; r denotes the regularity index of the true solution; and C_1 and C_2 are constants independent of h and p. As per the tensor-product structure of the NURBS basis functions, Eq. (3), the polynomial degree in the inequalities above, Eqs. (50), is actually $p = \min_i\{p_i\}$ for $i = \xi, \eta$.

For some manufactured solution, φ^{gk}, the (semi-)analytical anisotropic manufactured source, q_x^{gk}, can be evaluated for $g = 1, \ldots, G$ and for $k = 1, \ldots, K$:

$$Q^{gk} q_x = (L^{gk} - Q^{gk} S^{gk})\varphi; \tag{51}$$

where Q is the operator that acts group-ordinate-wise as defined in Eq. (14); and q_x is the left-hand side of the FONT-S_N equation; i.e. for $g = 1, \ldots, G$ and for $k = 1, \ldots, K$:

$$q_x^{gk} = \vec{\Omega}^k \cdot \vec{\nabla}\varphi^{gk} + \Sigma_t^g \varphi^{gk} - \sum_{g'=1}^{G} \Sigma_{s0}^{g' \to g} Y_0^0(\vec{\Omega}^k) \Phi_0^{g'0}. \tag{52}$$

The manufactured solution and source are used to study the convergence rates of the uniform refinement of a Cartesian mesh; and then of a more challenging pin-cell mesh. The coarsest meshes for both of the MMS verification test cases, defined over $V = [0,1]^2$, are presented in Fig. 1.

Table 1
The nuclear data for the 2D 1G MMS verification test case.

Material	g	Σ_t^g (cm^{-1})	$\Sigma_{s0}^{g\to 1}$ (cm^{-1})
(1) -	1	1.000E+00	5.000E−01

Table 2
The asymptotic orders of accuracy, Eqs. (50), for the MMS verification of the uniform refinement of the SIP-DG-IGA 1G SAAF-S_4 equation over a 2D Cartesian mesh; the convergence rates are evaluated as the slope of the last few points from each dataset.

	p	KI-1		KI-h	
		ϵ_{H^1}	ϵ_{L_2}	ϵ_{H^1}	ϵ_{L_2}
($n=0$)	1	1.00	2.00	1.00	2.00
	2	2.00	3.01	2.00	3.00
	3	2.98	3.99	3.00	4.00
($n=1$)	1	1.04	1.99	1.04	1.99
	2	2.02	3.02	2.00	3.05
	3	3.01	4.03	3.00	4.01
($n=2$)	1	1.09	1.98	1.09	1.98
	2	2.07	3.04	2.02	3.03
	3	3.06	4.09	3.00	4.03

Table 3
The nuclear data for the 2D 2G MMS verification test case.

Material	g	Σ_t^g (cm^{-1})	$\Sigma_{s0}^{g\to 1}$ (cm^{-1})	$\Sigma_s^{g\to 2}$ (cm^{-1})
(1) -	1	1.000E+00	5.000E−01	2.500E−01
(1) -	2	1.000E+00	0.000E+00	5.000E−01

5.1.1. MMS verification test case: A Cartesian mesh

The first MMS verification test case consists of a Cartesian mesh defined over $V = [0,1]^2$. It comprises a homogeneous material whose properties are prescribed in Table 1. The coarsest mesh is composed of four equal-volume bilinear NURBS patches. Assuming a *one-speed*, or one-group (1G), energy approximation and the S_4 Gauss–Chebyshev angular quadrature set, the manufactured solution is chosen for $k = 1, \dots, K$:

$$\begin{cases} \varphi^{nk}(\vec{r}) \;= \sin(B_x^n x)\sin(B_y^n y)\left[1+\vec{\Omega}^k\cdot\vec{\Omega}^k\right], & \vec{r}\in V; \quad \text{(a)} \\ B_x^n,\, B_y^n \;:= (2n{+}1)\pi, & \forall n\geq 0; \quad \text{(b)} \end{cases} \tag{53}$$

with

$$\Phi_0^0(\vec{r}) \approx \sum_{k=1}^{K} w_k Y_0^0(\vec{\Omega}^k)\sin(B_x^n x)\sin(B_y^n y)\left[1+\vec{\Omega}^k\cdot\vec{\Omega}^k\right], \tag{54}$$

$$\approx \sin(B_x^n x)\sin(B_y^n y)\sum_{k=1}^{K} w_k Y_0^0(\vec{\Omega}^k)\left[1+\vec{\Omega}^k\cdot\vec{\Omega}^k\right]; \tag{55}$$

where φ^{nk} denotes an odd harmonic mode as characterized by the geometric buckling, B_x^n and B_y^n. To allow for the maximum attainable convergence rates, the manufactured solution has been chosen to be smooth, yet, it cannot be arbitrarily represented exactly by higher-order NURBS bases. Moreover, the homogeneous Dirichlet (vacuum) boundary condition is naturally satisfied. One emphasizes that the manufactured solution is chosen for the within-angle equation rather than the full NTE; and thus, it is used to isolate those errors that result from the spatial discretization [59].

Uniform refinement. For the KI-refinement of linear, quadratic and cubic B-splines, the H^1-errors for the SIP-DG-IGA spatial discretization are presented in Fig. 2 for the manufactured solution chosen as the first, third and fifth harmonics of a modified standing wave equation; q.v. Eq. (53). The suffixes -1 and -h, in the legend, denote KI-1-refinement and h-refinement, respectively. Qualitatively similar plots were obtained for the L_2-error; however, for brevity, these have not been presented. Under refinement, the discontinuous discretization scheme converges to the analytical solution; and asymptotically, they attain their theoretical orders of accuracy, as presented in Table 2.

These results are qualitatively similar to those obtained for the verification of the SIP-DG-IGA discretization of the NDE presented by Wilson et al.; and thus, for brevity, the discussion is not repeated here [28].

5.1.2. MMS verification test case: A pin-cell mesh

The second MMS verification test case consists of a more-challenging, nuclear fuel pin-cell mesh defined over $V = [0,1]^2$. It comprises a homogeneous material whose properties are prescribed in Table 3. The coarsest mesh is composed of *nine* equal-volume

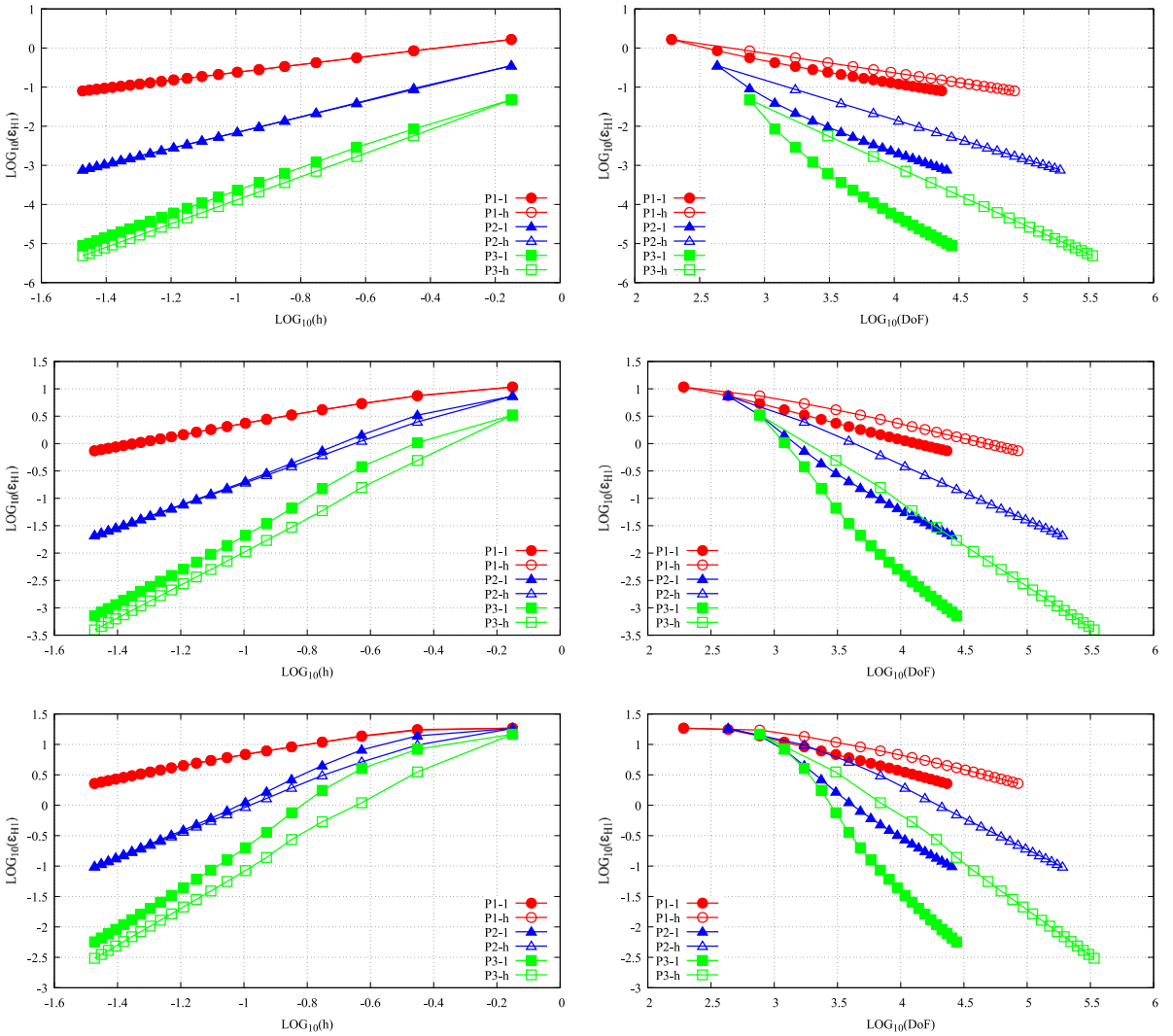

Fig. 2. The convergence plots, ϵ_{H^1} v h (left) and ϵ_{H^1} v DoFs (right), for the MMS verification of the uniform refinement of the SIP-DG-IGA 1G SAAF-S_4 equation over a 2D Cartesian mesh. The manufactured solution is chosen as per Eq. (53) for $n = 0$ (top row), $n = 1$ (middle row) and $n = 2$ (bottom row). (*Vide* the web-based version for reference to color.)

non-degenerate bi-quadratic NURBS patches. Assuming a two-group (2G) energy approximation and the S_4 Level Symmetric angular quadrature set, the manufactured solution is chosen for $k = 1, \ldots, K$:

$$\begin{cases} \varphi^{gk}(\vec{r}) = \cos(B_x^g x)\cos(B_y^g y)\left[1 + \vec{\Omega}^k \cdot \vec{\Omega}^k\right], & \vec{r} \in V; \quad \text{(a)} \\ B_x^g, B_y^g := (2g+1)\pi, & \text{for } g = 1, 2; \quad \text{(b)} \end{cases} \tag{56}$$

with

$$\Phi_l^{gm}(\vec{r}) \approx \sum_{k=1}^{K} w_k Y_l^m(\vec{\Omega}^k)\cos(B_x^{gk} x)\cos(B_y^{gk} y)\left[1 + \vec{\Omega}^k \cdot \vec{\Omega}^k\right], \tag{57}$$

$$\approx \cos(B_x^{gk} x)\cos(B_y^{gk} y)\sum_{k=1}^{K} w_k Y_l^m(\vec{\Omega}^k)\left[1 + \vec{\Omega}^k \cdot \vec{\Omega}^k\right]; \tag{58}$$

where φ^{gk} denotes an odd harmonic mode as characterized by the geometric buckling, B_x^g and B_y^g. Again, the manufactured solution has been chosen to be infinitely differentiable. However, now, the non-homogeneous Dirichlet reflective boundary condition is naturally satisfied.

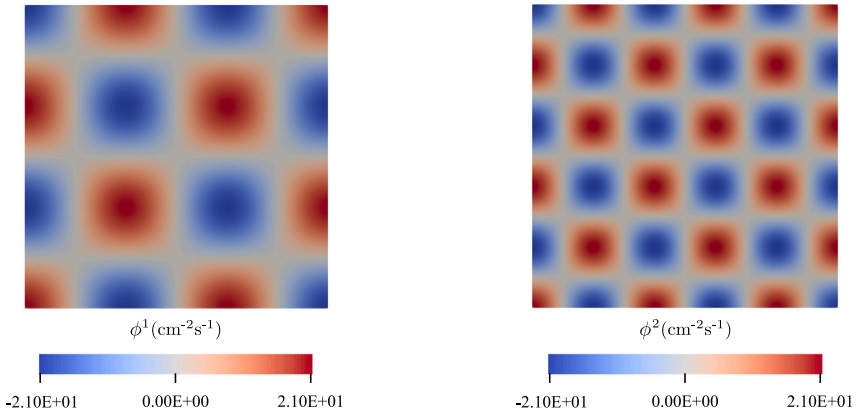

Fig. 3. The spatial distribution of the multi-group components of the neutron scalar flux for the 2G SAAF-S_4 equation over a 2D pin-cell mesh. The manufactured solutions are chosen as per Eq. (56) for $g = 1, 2$. (*Vide* the web-based version for reference to color.)

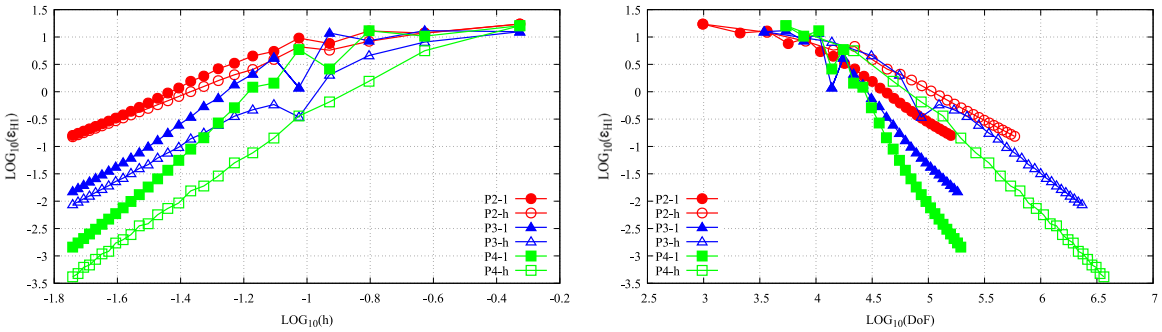

Fig. 4. The convergence plots, ϵ_{H^1} v h (left) and ϵ_{H^1} v DoFs (right), for the MMS verification of the uniform refinement of the SIP-DG-IGA 2G SAAF-S_4 equation over a 2D pin-cell mesh. The manufactured solutions are chosen as per Eq. (56) for $g = 1, 2$. (*Vide* the web-based version for reference to color.)

Table 4
The asymptotic orders of accuracy, Eqs. (50), for the MMS verification of the uniform refinement of the SIP-DG-IGA 2G SAAF-S_4 equation over a 2D pin-cell mesh. The convergence rates are evaluated as the slope of the last few points from each dataset.

p	KI-1		KI-h	
	ϵ_{H^1}	ϵ_{L_2}	ϵ_{H^1}	ϵ_{L_2}
2	2.24	3.54	2.03	3.01
3	3.31	4.43	3.02	4.00
4	4.48	5.36	4.04	5.04

The spatial distribution of the multi-group components of the neutron scalar flux for the 2G SAAF-S_4 equation over a 2D pin-cell mesh are presented in Fig. 3. The manufactured solutions are chosen as the third and fifth harmonics of a modified standing wave equation; q.v. Eq. (56) for $g = 1, 2$.

Uniform refinement. For the KI-refinement of quadratic, cubic and quartic NURBS bases, the H^1-errors for the SIP-DG-IGA spatial discretization are presented in Fig. 4 for the multi-group components of the manufactured solution chosen as the third and fifth harmonics of the standing wave equation; q.v. Eq. (56). Qualitatively similar plots were obtained for the L_2-error; however, for brevity, these have not been presented. Under refinement, the discontinuous discretization scheme converges to the analytical solution; and asymptotically, it attains the theoretical orders of accuracy for h-refinement, as presented in Table 4. However, for KI-1-refinement, one remarks a degree of super-convergence, which may be explained by the higher-order continuity in the basis.

5.2. Reed's 1D problem

Reed's nuclear reactor physics benchmark verification test case for the *one-speed* FONT-S_8 is posed over a heterogeneous slab that presents *four* regions of physically distinct materials, including a fuel, a can, a void and a moderator; v. Fig. 5. The corresponding macroscopic nuclear cross-section data are given in Table 5 [60]. The strengths of *two* different extraneous sources of neutrons are

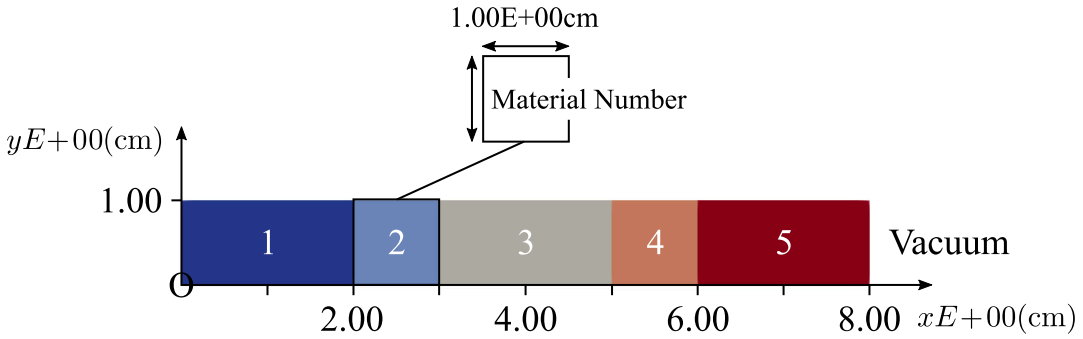

Fig. 5. The geometry for Reed's 1D 1G problem, which has been adapted from the original problem and presented in 2D. The constituent materials are denoted by the numbers in parentheses; viz. fuel (1), can (2), void (3) and moderator with a source (4) and without (5). (*Vide* the web-based version for reference to color.)

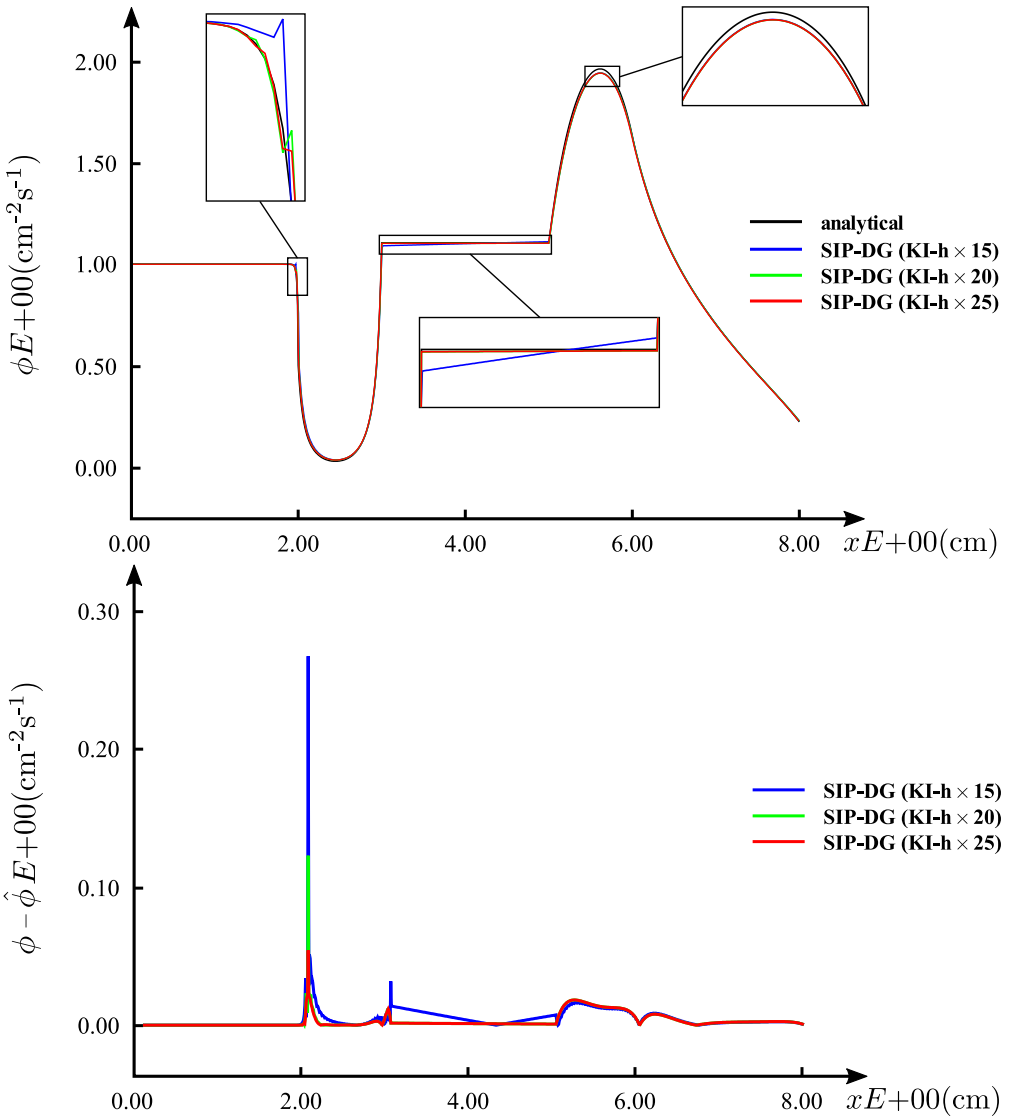

Fig. 6. The numerical solutions (top) to the SIP-DG-IGA 1G SAAF-S_8 equation and the corresponding discretization errors (bottom), $\phi - \hat{\phi}$, for different levels of uniform h-refinement for Reed's 1D problem. The unresolved boundary layer, $x = 2.0$ cm, the void region, $3.0 < x < 5.0$ cm, and the peak, $x \approx 6.0$ cm, are magnified. (*Vide* the web-based version for reference to color.)

Table 5
The nuclear data for Reed's 1D 1G problem [60].

Material	g	Σ_t^g (cm^{-1})	$\Sigma_{s0}^{g\to 1}$ (cm^{-1})	q_x^g (cm^{-3} s^{-1})
(1) Fuel	1	5.000E+01	0.000E+00	5.000E+01
(2) Can	1	5.000E+00	0.000E+00	0.000E+00
(3) Void	1	0.000E+00	0.000E+00	0.000E+00
(4) Moderator	1	1.000E+00	9.000E−01	1.000E+00
(5) Moderator	1	1.000E+00	9.000E−01	0.000E+00

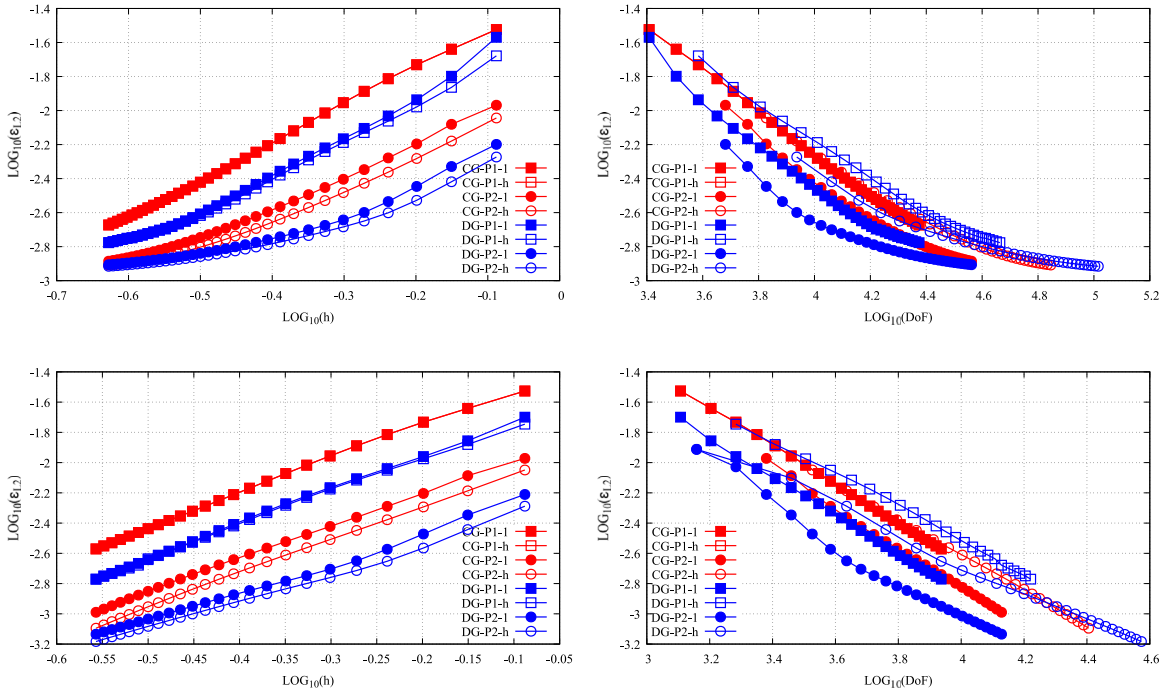

Fig. 7. The convergence plots, ϵ_{L_2} v h (left) and ϵ_{L_2} v DoFs (right), for the uniform refinement of the CBG-IGA and the SIP-DG-IGA 1G SAAF-S_8 equation for Reed's 1D problem; over the entire domain (top), $0 \le x \le 8$ cm, and over the can-and-void region (bottom), $2 \le x \le 5$ cm. (*Vide* the web-based version for reference to color.)

assigned between 0.00 cm $< x <$ 2.00 cm and 5.00 cm $< x <$ 6.00 cm. One prescribes reflective and vacuum boundary conditions at $x = 0.00$ cm and $x = 8.0$ cm, respectively; and since this problem has been adapted into 2D, reflective boundary conditions are also prescribed at $y = 0.00$ cm and $y = 1.00$ cm. The coarsest Cartesian mesh is constructed from *eight* bilinear NURBS patches. As determined by Warsa, with the help of MAPLE, a symbolic algebra program, there does exist an analytical solution to the mono-group component of neutron scalar flux for Reed's 1D problem; v. Fig. 6 [61].

This problem was selected to investigate further the convergence properties of the SIP-DG-IGA SAAF-S_N equation; more specifically, to determine the advantages, if any, for allowing discontinuities in the solution over a highly heterogeneous configuration. As such, only uniform h-refinement is performed with additional knots inserted solely in the ξ/x-direction.

To model the void region, one employs a low-density macroscopic cross-section of total collision, $\Sigma_{t,3} \approx \tau = 1.00\text{E}{-}06$ cm^{-1}; and to retain the SPD properties of the discrete linear systems, no other attempt is made to incorporate any sophisticated void treatment [35,36]. One recalls that the penalty parameters for the SIP-DG-IGA discretization vary as $\mu_f \propto 1/\Sigma_t$; q.v. Section 4. Therefore, to avoid any over-penalization of coarser meshes over the void region, one introduces the following modification $1/\Sigma_t^* = \min\{1/\tau, 1/h\}$, such that $1/\Sigma_t^* \to \infty$ as $\tau, h \to 0$.

For various degrees of h-refinement, the neutron scalar flux profiles for the SIP-DG-IGA SAAF-S_8 equation are presented in Fig. 6 along with their respective discretization error distributions. The corresponding convergence plots are presented in Fig. 7, including for KI-1-refinement, which is denoted in the legend by the suffix -1; and these are compared against a standard CBG-IGA discretization over similar spatial meshes. The discontinuous and the continuous Galerkin discretizations are denoted in the legend by the prefixes DG- and CG-, respectively. Clearly, it is advantageous to allow for discontinuities in the solution about the material interfaces; and especially so for the KI-1-refinement of coarser meshes over the void region where the SIP-DG-IGA discretization becomes competitive on a per DoF basis.

Since the analytical solution presents discontinuous first-order derivatives, one does not expect to attain full rates of convergence. In fact, the errors attributed to the unresolved boundary layer at $x = 2.0$ cm are negligibly small under refinement. However,

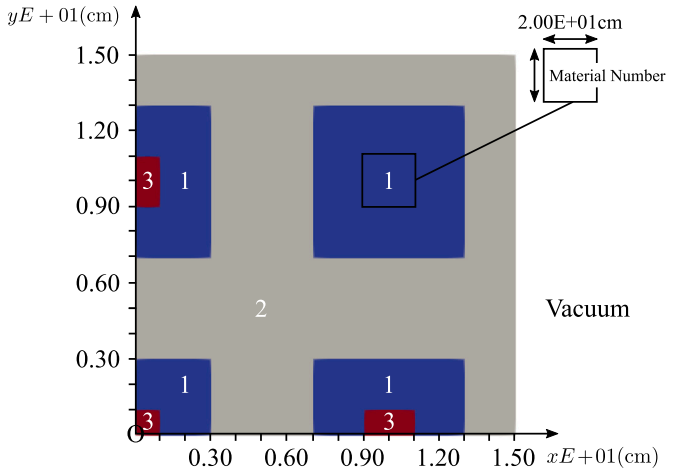

Fig. 8. The geometry for Ackroyd's 2D 1G small reactor problem [62]. The constituent materials are denoted by the numbers in parentheses; viz. fuel (1), moderator (2) and control-rod (3). (*Vide* the web-based version for reference to color.)

Table 6
The nuclear data for Ackroyd's 2D 1G small reactor problem [62].

Material	g	Σ_t^g (cm^{-1})	$\Sigma_{s0}^{g\to 1}$ (cm^{-1})	q_x^g (cm^{-3} s^{-1})
(1) Fuel	1	1.51461E−01	8.93030E−02	1.48083E−02
(2) Moderator	1	1.48934E−01	9.93430E−02	0.00000E+00
(3) Control-Rod	1	1.50000E+00	0.00000E+00	0.00000E+00

Table 7
The total solution times for the uniform KI-refinement of the SIP-DG-IGA 1G SAAF-S_2, S_4 & S_8 equations, for an increasingly large polynomial degree of the NURBS basis, p, for Ackroyd's 2D small reactor problem. These timings for the discontinuous discretization, denoted by DG, are compared to a standard CBG-IGA discretization, denoted by CG. All timings are provided in seconds.

		S_2		S_4		S_8	
		CG	DG	CG	DG	CG	DG
($p=1$)	KI-1 × 5	0.719	1.70	1.76	5.48	6.14	19.6
	KI-h × 5	0.719	8.99	1.76	37.0	6.14	111
($p=2$)	KI-1 × 5	4.57	8.74	12.7	29.7	44.2	99.6
	KI-h × 5	12.1	55.9	27.8	301	77.9	896
($p=3$)	KI-1 × 5	17.8	40.9	50.4	129	172	403
	KI-h × 5	41.4	229	145	885	503	2870
($p=4$)	KI-1 × 5	47.6	102	124	292	426	1030
	KI-h × 5	273	–	634	–	2060	–
($p=5$)	KI-1 × 5	99.8	221	261	718	972	2520
	KI-h × 5	–	–	–	–	–	–
($p=6$)	KI-1 × 5	242	–	662	–	2320	–
	KI-h × 5	–	–	–	–	–	–

modeling the void region with low-density cross-sections and no scatter implies that there must be some absorption of neutrons; and thus, owing to a lack of neutrons traveling in the positive x-direction, the result is an underestimation of the peak at $x \approx 6.0$ cm; where one notes that the corresponding discretization error appears to be constant under refinement. As such, the numerical solutions do not converge to the analytical one.

5.3. Ackroyd's 2D small reactor problem

Embedded in a moderator and enclosed by a bare surface, Ackroyd's small nuclear reactor physics benchmark verification test case consists of *four* fuel clusters with *three* control-rods inserted; as represented by Materials 2, 1 and 3, respectively; v. Fig. 8 [62]. The corresponding macroscopic nuclear cross-section data are provided in Table 6. Modeling for only a single thermal energy group, one assumes a uniformly dispersed and isotropic slowing-down source across the fueled regions. As per the *one-quarter* symmetry in the problem, reflective boundary conditions are prescribed at $x = y = 0.00$ cm. The coarsest Cartesian mesh is constructed from 225 bilinear NURBS patches. For the quantity of interest (QoI) chosen as the absorption in Material 1 in the top right-hand corner

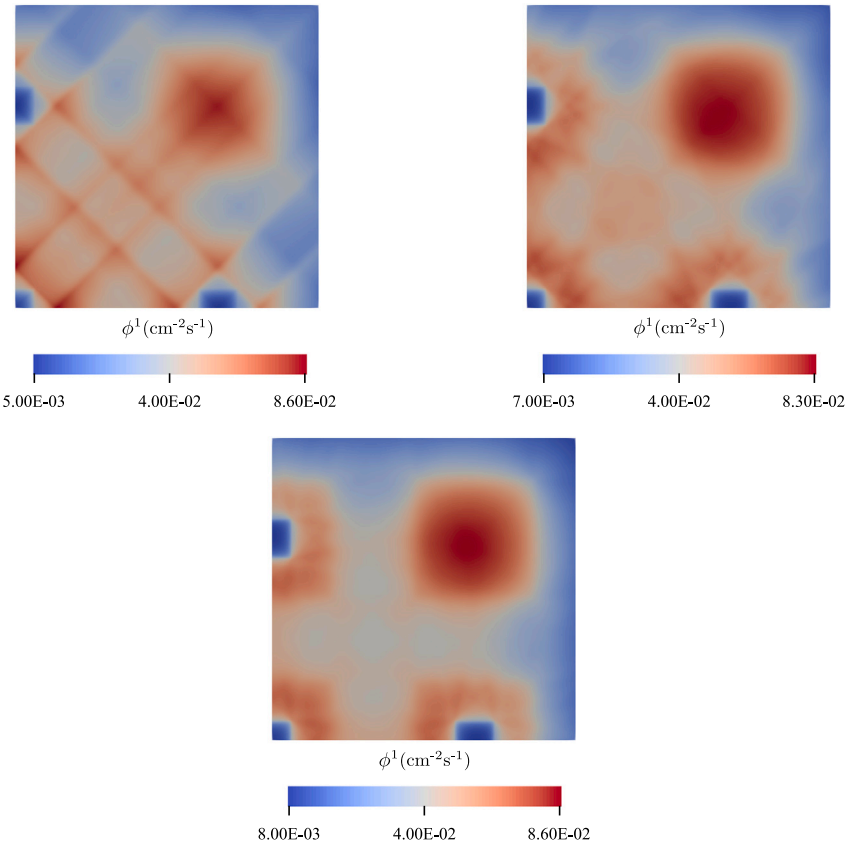

Fig. 9. The spatial distribution of the mono-group component of the neutron scalar flux for the 1G SAAF-S_N equation for Ackroyd's 2D small reactor problem; for S_2 (top left), S_4 (top right) and S_8 (bottom) Gauss–Chebyshev angular quadrature sets. The QoI is the absorption in Material 1 in the top right-hand corner; v. Fig. 8. (*Vide* the web-based version for reference to color.)

of Fig. 8, P_{N-1} reference solutions were obtained using the EVen Parity Neutron Transport (EVENT) code over a mesh of 104,000 bi-quadratic Lagrangian finite elements [63]. The finite element mesh was generated using transfinite interpolation mesh generation algorithms implemented within GEM, which is the mesh generator and data pre-processing software for EVENT [64].

The spatial distribution of the mono-group component of the neutron scalar flux for the S_2, S_4 & S_8 approximations with Gauss–Chebyshev angular quadrature sets are presented in Fig. 9. Those errors due to the spatial discretization can be strongly coupled to the angular discretization; and especially so for dominating ray effects [65]. Whilst much less apparent for the SAAF-S_8, the ray effects are clearly visible in solution for smaller angular quadrature sets; and unsurprisingly, accurate numerical solutions demand good resolution along these rays.

Owing to the potential for higher-order continuity across knot-spans, $C^{p-\vec{m}}$, NURBS-based IGA discretizations of smooth, elliptic problems can exhibit improved numerical accuracy per DoF when compared to other FEM-like discretizations over similar meshes [23,66]. Indeed, this is observed in Fig. 10, where KI-1-refinement consistently yields more accuracy in the QoI, which is a local quantity, per DoF than *h*-refinement for each of the increasingly large angular quadrature sets; and for each of the bases of linear, quadratic and cubic NURBS functions. However, the individual group-ordinate-wise banded matrices do become increasingly more ill conditioned for increasingly large polynomial degrees; and increasingly more computational effort is required to converge the within-group within-angle equations since the algebraic multi-grid pre-conditioner appears to become increasingly less effective for higher-order NURBS bases.

The total solution times for a chosen uniform KI-refinement of the SIP-DG-IGA 1G SAAF-S_2, S_4 & S_8 equations, for an increasingly large polynomial degree of the NURBS basis, are presented in Table 7. These timings are indicative of the amount of serial computational effort required of a single MPI process to invert the ordinate-wise banded matrices that result from the proposed discontinuous spatial discretization, denoted by DG; and they are compared to the total solution times of a standard CBG-IGA discretization, denoted by CG, over the same spatial mesh. As an aside, one notes that the total analysis time is dominated by the solution time; and the other stages of the analysis, including refinement and assembly, contribute only slightly. Clearly, as the S_N order increases, there are more ordinate-wise banded matrices to invert; and so, the total solution time increases.

For ease of comparison, the average solution time required to invert each ordinate-wise system is plotted against the corresponding DoFs of the discrete system in Fig. 11 where each data point in each series represents an increase in the polynomial degree of

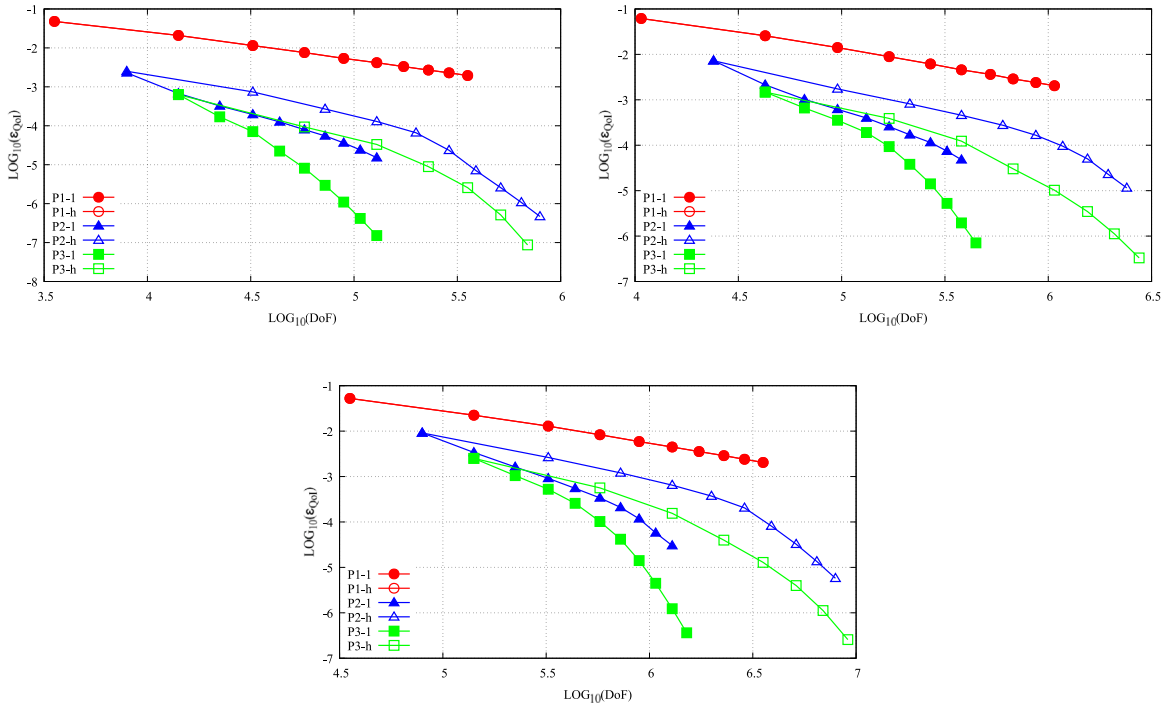

Fig. 10. The convergence plots, ϵ_{QoI} v DoFs, for the uniform refinement of the SIP-DG-IGA 1G SAAF-S_2 (top left), SAAF-S_4 (top right) and SAAF-S_8 (bottom) equations for Ackroyd's 2D small reactor problem. The QoI is the absorption in Material 1 in the top right-hand corner; v. Fig. 8. (*Vide* the web-based version for reference to color.)

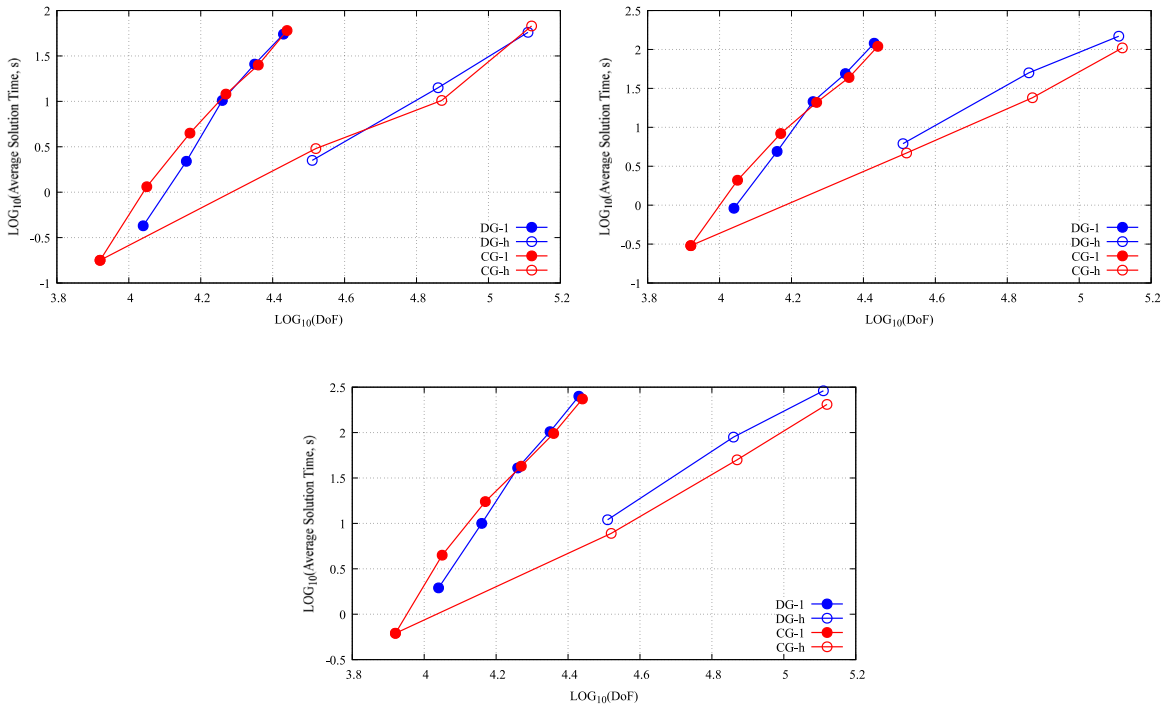

Fig. 11. The average solution times per ordinate-wise system for the uniform KI-refinement of the SIP-DG-IGA 1G SAAF-S_2 (top left), SAAF-S_4 (top right) and SAAF-S_8 (bottom) equations for Ackroyd's 2D small reactor problem; they are derived from those total solution times presented in Table 7. These timings for the discontinuous discretization, denoted by DG and presented in blue, are compared to a standard CBG-IGA discretization, denoted by CG and presented in red. (*Vide* the web-based version for reference to color.)

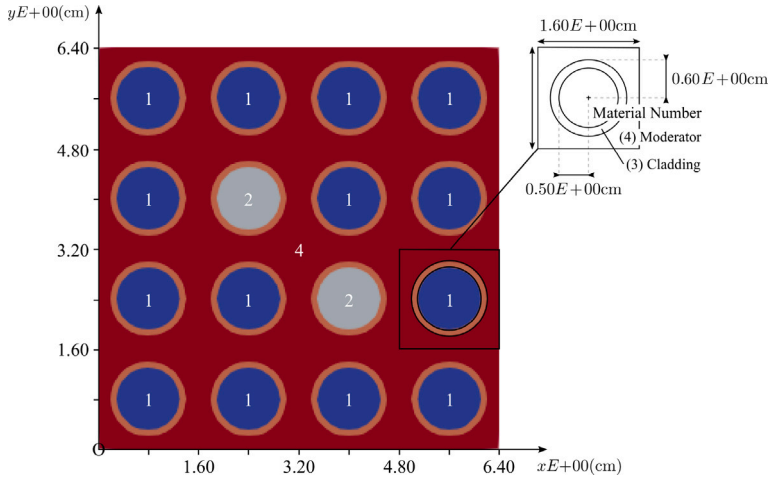

Fig. 12. The geometry for Hong and Cho's 2D 2G BWR problem with burnable Gadolinium poison pins [67]. The constituent materials are denoted by the numbers in parentheses; viz. Uranium oxide (1), Uranium & Gadolinium Oxides (2), cladding (3) and moderator (4). (*Vide* the web-based version for reference to color.)

Table 8
The nuclear data for Hong and Cho's 2D 2G BWR problem with burnable gadolinium poison pins [67]. The fission spectrum is $\chi = [1.00, 0.00]^T$.

Material	g	Σ_t^g (cm^{-1})	$\Sigma_{s0}^{g\to1}$ (cm^{-1})	$\Sigma_{s0}^{g\to2}$ (cm^{-1})	Σ_f^g (cm^{-1})	$\nu^g\Sigma_f^g$ (cm^{-1})
(1) UO_2	1	3.62022E−01	3.33748E−01	6.64881E−04	7.22964E−03	1.86278E−02
	2	5.72155E−01	0.00000E+00	3.80898E−01	1.41126E−01	3.44137E−01
(2) UO_2 & Gd_2O_2	1	3.71785E−01	3.38096E−01	6.92807E−04	6.97904E−03	1.79336E−02
	2	1.75000E+00	0.00000E+00	3.83204E−01	6.47524E−02	1.57929E−01
(3) Cladding	1	2.74144E−01	2.72377E−01	1.90838E−04	0.00000E+00	0.00000E+00
	2	2.80890E−01	0.00000E+00	2.77230E−01	0.00000E+00	0.00000E+00
(4) Moderator	1	6.40711E−01	6.07382E−01	3.31316E−02	0.00000E+00	0.00000E+00
	2	1.69131E+00	0.00000E+00	1.68428E+00	0.00000E+00	0.00000E+00

the NURBS basis followed by KI-refinement. One recalls that the processes of *KI* and *DE* are not commutative [44]. Indeed, the timings presented in Table 7 were chosen to compare the continuous and discontinuous discretizations schemes on a similar per DoF basis; and one notes that they give comparable average timings for both KI-1-refinement and *h*-refinement.

In each case, there is a non-linear effect on the average solution times from KI-refinement of the NURBS basis for an increasingly large polynomial degree, which may infer a degradation of the conditioning of the ordinate-wise matrices. The rate of increase in average solution time per DoF is more significant for KI-1-refinement than for *h*-refinement since the former quickly attains those timings of the latter for approximately an order-of-magnitude less DoFs. One recalls how *h*-refinement becomes increasingly more expensive to perform as the polynomial degree of the NURBS basis, *p*, increases.

5.4. Hong and Cho's 2D BWR problem

Hong and Cho's nuclear reactor physics benchmark verification test case is a four-by-four boiling water reactor (BWR) lattice with *two* adjacent burnable Gadolinium poison pins [67]. This problem presents *four* physically distinct regions, including 14 homogenized regular fuel pins (3wt.% UO_2) and *two* poisoned ones (3wt.% Gd_2O_3); each pin is encased in a cladding of Zr-2 and moderated by water, as represented by Materials 1, 2, 3 and 4, respectively; v. Fig. 12. For the two-group condensation of the 172-group WLUP nuclear data library at the delimitation of 4 eV, this problem was first modeled by DRAGON, a lattice code [68]. These few-group macroscopic neutron cross-section data are reproduced in Table 8 [69]. To model an infinite lattice, reflective boundary conditions are specified at every external physical boundary. The coarsest mesh is constructed from 208 bi-quadratic NURBS patches. For the QoI chosen as k_{eff}, Yang and Satvat provide a reference of $k_{eff} = 0.986561$ [69]. However, in this instance, a reference solution was obtained from a CBG-IGA discretization of the 2G SAAF-S_6 equation over energy-dependent meshes generated after the 11th iteration of a goal-based adaptive *hp*-refinement algorithm, which was implemented within the same framework that Wilson et al. applied to the multi-group NDE [27]; this will be presented in a subsequent paper.

The spatial distribution of the multi-group components of the neutron scalar flux for the 2G SAAF-S_6 equation with the Level Symmetric angular quadrature set are presented in Fig. 13. And, again, one observes in Fig. 14 that KI-1-refinement consistently yields more accuracy in the QoI, which is a global quantity, per DoF than *h*-refinement for a basis of quadratic, cubic and quartic

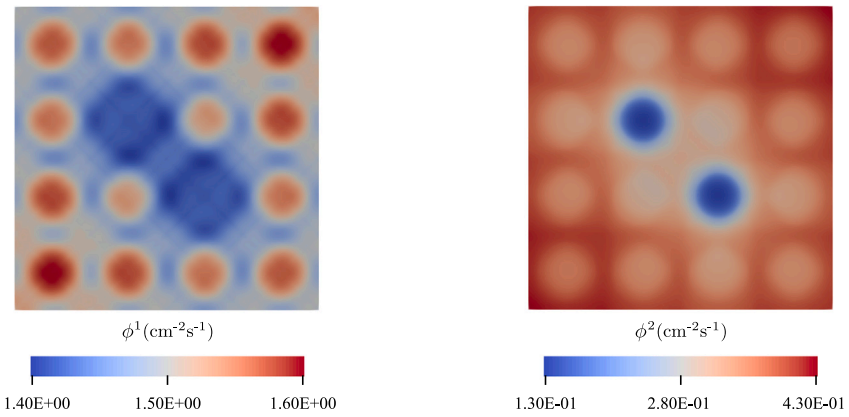

Fig. 13. The spatial distribution of the multi-group components of the neutron scalar flux for the 2G SAAF-S_6 equation for Hong and Cho's 2D BWR problem with burnable Gadolinium poison pins. The QoI is the k_{eff}. (*Vide* the web-based version for reference to color.)

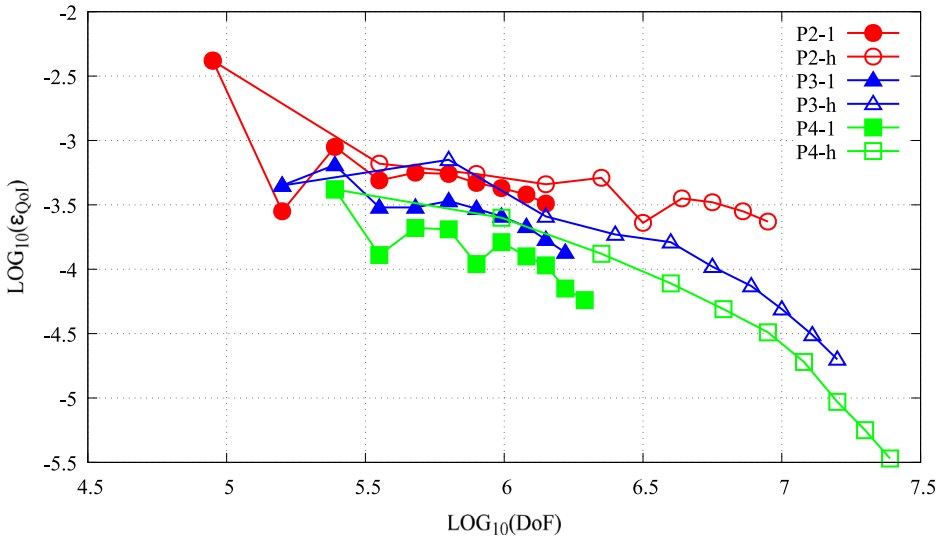

Fig. 14. The convergence plots, ϵ_{QoI} v DoFs, for the uniform refinement of the SIP-DG-IGA 2G SAAF-S_6 equation for Hong and Cho's 2D BWR problem with burnable Gadolinium poison pins. The QoI is the k_{eff}. (*Vide* the web-based version for reference to color.)

NURBS functions. Moreover, one recalls how *h*-refinement becomes increasingly more expensive to perform as the polynomial degree of the basis, *p*, increases. This is due to the fact that the number of unknowns is increased for every knot inserted; and knots must be inserted with a multiplicity of $\dot{m} = p + 1$ in order to render the basis discontinuous.

6. Conclusion

This paper presents the first application of a SIP-DG-IGA spatial discretization to the multi-group SAAF-S_N equation, which can be readily extended to full 3D heterogeneous nuclear reactor physics problems. Penalty parameters, based upon a coercivity analysis of the bilinear form, were derived for general element types to ensure sufficient, not excessive, penalization of the discrete solution field across the spatial mesh. The spatial discretization results in large, sparse, symmetric positive-definite (SPD) matrices that can benefit from PETSc's capacity for distributed-memory CRS data structures; and the parallel implementation of its PCG smoothers. However, it was observed that the algebraic multi-grid pre-conditioner was increasingly less effective for higher-order NURBS bases. Indeed, most efficient and well-established pre-conditioners have been developed for low-order continuity FEM; and they are not generally effective for bases that exhibit higher-order continuity [26,70].

Nonetheless, the proposed spatial discretization was shown to be consistent and convergent using the MMS and a series of nuclear reactor physics benchmark verification test cases that were analyzed in this paper. NURBS-based IGA discretizations of smooth, elliptic problems can exploit the potential for higher-order continuity across knot-spans. For bases of linear, quadratic, cubic and quartic NURBS functions, this paper shows that KI-1-refinement consistently yields improved numerical accuracy per degree of freedom (DoF) than *h*-refinement.

Despite incurring at least twice as many DoFs when compared to a standard continuous Bubnov–Galerkin discretization over similar spatial meshes, there are advantages to allowing discontinuities, or some degree of *disconnectedness*, in the numerical solution. This is especially important over heterogeneous problems where the neutron scalar flux may exhibit significant changes in its profile across material interfaces. Moreover, the proposed discontinuous scheme yields a more-compact spatial discretization stencil; and its flexibility lends itself to its implementation within self-adaptive, local-refinement algorithms, which will form the subject of subsequent research.

CRediT authorship contribution statement

S.G. Wilson: Writing – original draft, Software, Methodology, Investigation, Conceptualization. **M.D. Eaton:** Writing – review & editing, Supervision, Conceptualization. **J. Kópházi:** Writing – review & editing, Supervision.

Declaration of competing interest

The authors declare that they have no known competing financial interests or personal relationships that could have appeared to influence the work reported in this paper.

Data availability

In accordance with EPSRC funding requirements, all supporting data used to create figures in this paper may be accessed via the following URL: https://doi.org/10.5281/zenodo.11863256.

Acknowledgments

S. G. Wilson acknowledges the financial support of the Engineering and Physical Sciences Research Council (EPSRC) under their doctoral training partnership (DTP) scheme (EPSRC Grant No. EP/N509486/1). S. G. Wilson also acknowledges the financial support of Rolls-Royce, United Kingdom for the funding of the CASE conversion of the EPSRC DTP PhD. Finally, the authors would like to thank Dr Andrew Richards, director of research computing services (RCS) and the RCS group at Imperial College London (ICL) for their support in using the high-performance computing (HPC) facilities at ICL.

References

[1] L.E. Boltzmann, Weitere studien über das wärmegleichgewicht unter gasmolekülen, in: Sitzungsberichte der Mathematisch-Naturwissenschaftlichen Classe Kaiserlichen Akademie der Wissenschaften, Vol. 66, 1872, pp. 275–370, http://dx.doi.org/10.1007/978-3-322-84986-1_3.
[2] E.E. Lewis, W.F. Miller Jr., Computational Methods of Neutron Transport, American Nuclear Society, 1993.
[3] L.S. Ornstein, G.E. Uhlenbeck, Some kinetic problems regarding the motion of neutrons through parafine, Physica 4 (6) (1937) 478–486.
[4] O. Halpern, R. Lueneburg, O. Clark, On multiple scattering of neutrons I. Theory of the albedo of a plane boundary, Phys. Rev. 53 (1938) 173–183.
[5] R.K. Osborn, S. Yip, The Foundations of Neutron Transport Theory, Monograph Series on Nuclear Science and Technology, Gordon and Breach, 1966.
[6] I. Pazsit, A simple derivation of the neutron transport equation, Nucl. Sci. Eng. 112 (4) (1992) 369–374.
[7] V.S. Vladimirov, Mathematical Problems in the One-Velocity Theory of Particle Transport, Report No. AECL-1661, Atomic Energy of Canada Ltd. Translated from Transactions of the V. A. Steklov Mathematical Institute (1961), 1963.
[8] R.T. Ackroyd, Least-squares derivation of extremum and weighted-residual meethods for equations of reactor physics - I. The first-order Boltzmann equation and a first-order initial-value equation, Ann. Nucl. Energy 10 (1983) 65–99.
[9] G.C. Pomraning, M. Clark, The variational method applied to the monoenergetic Boltzmann equation, part II, Nucl. Sci. Eng. 16 (1963) 155–164.
[10] R.T. Ackroyd, A finite element method for neutron transport - I. Some theoretical considerations, Ann. Nucl. Energy 5 (1978) 75–94.
[11] J.E. Morel, J.M. McGhee, A self-adjoint angular flux equation, Nucl. Sci. Eng. 132 (1999) 312–325.
[12] A. Abdelfattah, V. Barra, N. Beams, R. Bleile, J. Brown, J.-S. Camier, R. Carson, N. Chalmers, V.A. Dobrev, Y. Dudouit, P. Fischer, A. Karakus, S. Kerkemeier, T. Kolev, Y.-H. Lan, E. Merzari, M. Min, M. Phillips, T. Rathnayake, R. Rieben, K. Weiss, GPU algorithms for efficient exascale discretizations, Parallel Comput. 108 (2021).
[13] D. Moxey, C.D. Cantwell, R.M. Kirby, S.J. Sherwin, Optimising the performance of the spectral/hp element method with collective linear algebra operations, Comput. Methods Appl. Mech. Engrg. 310 (2016) 628–645.
[14] R. Lohner, Cache-efficient renumbering for vectorization, Int. J. Numer. Methods Bioeng. 26 (2008) 628–636.
[15] R. Lohner, M. Galle, Minimization of indirect addressing for edge-based field solvers, Commun. Numer. Methods Eng. 18 (2002) 335–343.
[16] X. Xu, Implicit discrete ordinates discontinuous Galerkin method for radiation problems on shared-memory multicore CPU/many-core GPU computation architecture, Numer. Heat Transfer B 79 (2021) 165–188.
[17] C.M. Kang, K.F. Hansen, Finite element methods for reactor analysis, Nucl. Sci. Eng. 51 (1973) 456–495.
[18] K.F. Hansen, C.M. Kang, Finite element methods for reactor physics analysis, Adv. Nucl. Sci. Eng. 51 (1973) 456–495, http://dx.doi.org/10.13182/NSE73-A23278.
[19] E.H. Mund, Spectral element solutions for the p_N neutron transport equations, Comput. & Fluids 43 (2011) 102–106.
[20] A.R. Owens, J.A. Welch, J. Kópházi, M.D. Eaton, Discontinuous isogeometric analysis methods for the first-order form of the neutron transport equation with discrete ordinate (S_N) angular discretisation, J. Comput. Phys. 315 (2016) 501–535.
[21] A.R. Owens, J. Kópházi, M.D. Eaton, Energy dependent mesh adaptivity of discontinuous isogeometric discrete ordinate methods with dual weighted residual error estimators, J. Comput. Phys. 335 (2017) 352–386, http://dx.doi.org/10.1016/j.jcp.2017.01.035.
[22] J.A. Welch, J. Kópházi, A.R. Owens, M.D. Eaton, A geometry preserving, conservative, mesh-to-mesh isogeometric interpolation algorithm for spatial adaptivity of the multigroup, second-order even-parity form of the neutron transport equation, J. Comput. Phys. 347 (2017) 129–146, http://dx.doi.org/10.1016/j.jcp.2017.06.015.

[23] C. Latimer, J. Kópházi, M.D. Eaton, R.G. McClarren, A geometry conforming isogeometric method for the self-adjoint angular flux (SAAF) form of the neutron transport equation with a discrete ordinate (s_N) angular discretisation, Ann. Nucl. Energy 136 (2020) 107049, http://dx.doi.org/10.1016/j.anucene.2019.107049.

[24] J.A. Ferguson, J. Kópházi, M.D. Eaton, R.G. McClarren, Virtual element methods for the spatial discretisation of the multigroup neutron diffusion equation on polygonal meshes with applications to nuclear reactor physics, Ann. Nucl. Energy 151 (2021) http://dx.doi.org/10.1016/j.anucene.2020.107884.

[25] J.A. Ferguson, J. Kópházi, M.D. Eaton, R.G. McClarren, NURBS enhanced virtual element methods for the spatial discretization of the multigroup neutron diffusion equation on curvilinear polygonal meshes, J. Comput. Theor. Transp. 51 (4) (2022) 145–204, http://dx.doi.org/10.1080/23324309.2022.2103150.

[26] K.P.S. Gahaluat, J.K. Kraus, S.K. Tomar, Multigrid methods for isogeometric discretisation, Comput. Methods Appl. Mech. Engrg. 253 (2013) 413–425, http://dx.doi.org/10.1016/j.cma.2012.08.015.

[27] S.G. Wilson, M.D. Eaton, J. Kópházi, Energy-dependent, self-adaptive mesh $h(p)$-refinement of a constraint-based continuous bubnov-Galerkin isogeometric analysis spatial discretization of the multi-group neutron diffusion equations with dual-weighted residual error measures, J. Comput. Theor. Transp. 53 (2024) 89–152, http://dx.doi.org/10.1080/23324309.2024.2313460.

[28] S.G. Wilson, M.D. Eaton, J. Kópházi, Energy-dependent, self-adaptive mesh $h(p)$-refinement of an interior-penalty scheme for a discontinuous Galerkin isogeometric analysis spatial discretisation of the multi-group neutron diffusion equations with dual-weighted residual error measures, J. Comput. Theor. Transp. 53 (2024) 223–278, http://dx.doi.org/10.1080/23324309.2024.2334277.

[29] H. Hurwitz Jr., R. Ehrlich, Multigroup Methods for Neutron Diffusion Problems, Report No. HECD-3595, Knolls Atomic Power Laboratory, 1953.

[30] S. Chandrasekhar, Radiative Transfer, Oxford University Press, 1950.

[31] B.G. Carlson, Solution of the Transport Equation by S_N Approximations, Tech. rep., Los Alamos Scientific Laboratory of the University of California, 1953.

[32] C. Lee, The Discrete S_N Approximation to Transport Theory, Report No. LA-2595, Los Alamos National Laboratory, 1961.

[33] H.R. Hammer, J.E. Morel, Y. Wang, A weighted least-squares transport equation compatible with source iteration and voids, Nucl. Sci. Eng. 193 (4) (2019) 388–403.

[34] R.T. Ackroyd, J.G. Issa, N.S. Riyait, Treatment of voids in finite element transport methods, Prog. Nucl. Energy 18 (1–2) (1986) 85–89.

[35] Y. Wang, H. Zhang, R.C. Martineau, Diffusion acceleration schemes for self-adjoint angular flux formulation with a void treatment, Nucl. Sci. Eng. 176 (2) (2014) 201–225.

[36] S. Schunert, Y. Wang, R. Martineau, M.D. DeHart, A new mathematical adjoint for the modified SAAF-s_N equations, Ann. Nucl. Energy 75 (2015) 340–352, http://dx.doi.org/10.1016/j.anucene.2014.08.028.

[37] M.A. Abbott, An Introduction to the Method of Characteristics, Thames and Hudson, 1966.

[38] J.D. Hoffman, Numerical Methods for Engineers and Scientists, second ed., Marcel Dekker, Inc., 2001.

[39] S.G. Wilson, Self-Adaptive Isogeometric Spatial Discretisations of the First and Second-Order Forms of the Neutron Transport Equation with Dual-Weighted Residual Error Measures and Diffusion Acceleration (Ph.D. thesis), Imperial College London, 2021, http://dx.doi.org/10.25560/105670.

[40] S.G. Wilson, J. Kópházi, A.R. Owens, M.D. Eaton, Interior penalty schemes for discontinuous isogeometric methods with an application to nuclear reactor physics, in: Proc. of the International Conference of Nuclear Engineering, ICONE26, 3: Nuclear Fuel and Material, Reactor Physics and Transport Theory, ASME, 2018, http://dx.doi.org/10.1115/ICONE26-81322.

[41] A.R. Owens, J. Kópházi, M.D. Eaton, Optimal trace inequality constants for interior penalty discontinuous Galerkin discretisations of elliptic operators using arbitrary elements with non-constant Jacobians, J. Comput. Phys. 350 (2017) 847–870, http://dx.doi.org/10.1016/j.jcp.2017.09.020.

[42] M.G. Cox, The numerical evaluations of B-splines, IMA J. Appl. Math. 10 (1972) 134–149, http://dx.doi.org/10.1093/imamat/10.2.134.

[43] C. de Boor, On calculating with B-splines, J. Approx. Theory 6 (1972) 50–62, http://dx.doi.org/10.1016/0021-9045(72)90080-9.

[44] J. Cottrell, T. Hughes, A. Reali, Studies of refinement and continuity in isogeometric structural analysis, Comput. Methods Appl. Mech. Engrg. 196 (2007) 4160–4183, http://dx.doi.org/10.1016/j.cma.2007.04.007.

[45] J.J. Duderstadt, W.R. Martin, Transport Theory, John Wiley & Sons, Inc., 1979.

[46] J.T. Oden, J.N. Reddy, An Introduction to the Mathematical Theory of Finite Elements, Dover Publications, 2011.

[47] A. Ern, J. Guermond, Theory and Practice of Finite Elements, Applied Mathematical Sciences, vol. 159, Springer, 2004, http://dx.doi.org/10.1007/978-1-4757-4355-5.

[48] F. Brezzi, B. Cockburn, L. Marini, E. Süli, Stabilization mechanisms in discontinuous Galerkin finite element methods, Comput. Methods Appl. Mech. Engrg. 195 (2006) 3293–3310, http://dx.doi.org/10.1016/j.cma.2005.06.015.

[49] J.S. Hesthaven, T. Warburton, Nodal Discontinuous Galerkin Methods: Algorithms, Analysis and Applications, Texts in Applied Mathematics, vol. 54, Springer, 2010, http://dx.doi.org/10.1007/978-0-387-72067-8.

[50] D.A. Di Pietro, A. Ern, Mathematical Aspects of Discontinuous Galerkin Methods, Mathémathiques et Applications, vol. 69, Springer, 2012, http://dx.doi.org/10.1007/978-3-642-22980-0.

[51] K. Shahbazi, An explicit expression for the penalty parameter of the interior penalty method, J. Comput. Phys. 205 (2005) 401–407, http://dx.doi.org/10.1016/j.jcp.2004.11.017.

[52] M. Drosson, K. Hillewaert, On the stability of the symmetric interior penalty method for the Spalart-Allmaras turbulence model, J. Comput. Appl. Math. 246 (2013) 122–135, http://dx.doi.org/10.1016/j.cam.2012.09.019.

[53] W. Pazner, T. Kolev, Uniform subspace correction preconditioners for discontinuous Galerkin methods with $h(p)$-refinement, Commun. Appl. Math. Comput. 4 (2022) 697–727, http://dx.doi.org/10.1007/s42967-021-00136-3.

[54] M. Metcalf, J. Reid, M. Cohen, R. Bader, Modern Fortran Explained: Incorporating Fortran 2023, Sixth ed., Numerical Mathematics and Scientific Computation, Oxford University Press, 2023.

[55] S. Balay, S. Abhyankar, M. Adams, J. Brown, P. Brune, K. Buschelman, L. Dalcin, V. Eijkhout, W. Gropp, D. Karpeyev, D. Kaushik, M. Knepley, D. May, L.C. McInnes, R. Mills, T. Munson, K. Rupp, P. Sanan, B. Smith, S. Zampini, H. Zhang, H. Zhang, PETSc Users Manual: Revision 3.9, Report No. ANL-95/11 Rev. 3.9,, Argonne National Laboratory, 2018.

[56] V.E. Henson, U.M. Yang, BoomerAMG: A parallel algebraic multigrid solver and preconditioner, Appl. Numer. Math. 41 (2002) 155–177, http://dx.doi.org/10.1016/S0168-9274(01)00115-5.

[57] K. Salari, P. Knupp, Code Verification by the Method of Manufactured Solutions, Report No. SAND2000-1444, Sandia National Laboratories, 2000, http://dx.doi.org/10.2172/759450.

[58] B. Rivière, Discontinuous Galerkin methods for solving elliptic and parabolic equations: Theory and Implementation, Frontiers in Applied Mathematics, SIAM, 2008, http://dx.doi.org/10.1137/1.9780898717440.

[59] J.S. Warsa, A continuous finite element-based, discontinuous finite element method for s_N transport, Nucl. Sci. Eng. 160 (2008) 385–400, http://dx.doi.org/10.13182/NSE160-385TN.

[60] W.H. Reed, New difference schemes for the neutron transport equation, Nucl. Sci. Eng. 46 (2) (1971) 309–314, http://dx.doi.org/10.13182/NSE46-309.

[61] J.S. Warsa, Analytical (S_N) solutions in heterogeneous slabs using symbolic algebra computer programs, Ann. Nucl. Energy 29 (2002) 851–874.

[62] R.T. Ackroyd, Finite Element Methods for Particle Transport: Applications to Reactor and Radiation Physics. 6, Research Studies in Nuclear Technology, 1997.

[63] C.R.E. de Oliveira, An arbitrary geometry finite element method for multigroup neutron transport with anisotropic scattering, Prog. Nucl. Energy 18 (1–2) (1986) 227–236.

[64] J. Wood, M.M.R. Williams, Recent progress in the application of the finite element method to the neutron transport equation, Prog. Nucl. Energy 14 (1) (1984) 21–40.
[65] A.R. Owens, J.A. Welch, J. Kópházi, M.D. Eaton, An adaptive, hanging-node, discontinuous isogeometric analysis method for the first-order form of the neutron transport equation with discrete ordinate (S_N) angular discretisation, Comput. Methods Appl. Mech. Engrg. 318 (2017) 215–241, http://dx.doi.org/10.1016/j.cma.2017.01.036.
[66] J.A. Welch, J. Kópházi, A.R. Owens, M.D. Eaton, Isogeometric analysis for the multigroup neutron diffusion equation with applications in reactor physics, Ann. Nucl. Energy 101 (2017) 465–480, http://dx.doi.org/10.1016/j.anucene.2016.11.015.
[67] S.G. Hong, N.Z. Cho, CRX: A code for rectangular and hexagonal lattices based on the method of characteristics, Ann. Nucl. Energy 25 (8) (1998) 547–565.
[68] G. Marleau, A. Hébert, R. Roy, A User Guide for Dragon Version 5, Report No. IGE-335, Institut de Génie Nucléaire, 2019.
[69] X. Yang, N. Satvat, MOCUM: A two-dimensional method of characteristics code based on constructive solid geometry and unstructured meshing for general geometries, Ann. Nucl. Energy 46 (2012) 20–28.
[70] G. Sangalli, M. Tani, Isogeometric preconditioners based on fast solvers for the Sylvester equation, SIAM J. Sci. Comput. 38 (6) (2016) A3644–A3671, http://dx.doi.org/10.1137/16M1062788.